Monthly Notices
of the
ROYAL ASTRONOMICAL SOCIETY

MNRAS **492,** 1641–1670 (2020)
Advance Access publication 2019 December 16

doi:10.1093/mnras/stz3496

Homogeneous analysis of globular clusters from the APOGEE survey with the BACCHUS code – II. The Southern clusters and overview

Szabolcs Mészáros,[1,2,3]★ Thomas Masseron,[4,5] D. A. García-Hernández,[4,5] Carlos Allende Prieto,[4,5] Timothy C. Beers,[6] Dmitry Bizyaev,[7] Drew Chojnowski,[8] Roger E. Cohen,[9] Katia Cunha,[10,11] Flavia Dell'Agli,[4,5] Garrett Ebelke,[12] José G. Fernández-Trincado,[13,14] Peter Frinchaboy,[15] Doug Geisler,[16,17,18] Sten Hasselquist,[19]† Fred Hearty,[20] Jon Holtzman,[21] Jennifer Johnson,[22] Richard R. Lane,[23] Ivan Lacerna,[13,24] Penelopé Longa-Peña,[25] Steven R. Majewski,[12] Sarah L. Martell,[26] Dante Minniti,[27,28,29] David Nataf,[30] David L. Nidever,[31,32] Kaike Pan,[7] Ricardo P. Schiavon,[33] Matthew Shetrone,[34] Verne V. Smith,[32] Jennifer S. Sobeck,[11] Guy S. Stringfellow,[35] László Szigeti,[1,3] Baitian Tang,[36] John C. Wilson[12] and Olga Zamora[4,5]

Affiliations are listed at the end of the paper

Accepted 2019 December 10. Received 2019 December 10; in original form 2019 August 28

ABSTRACT

We investigate the Fe, C, N, O, Mg, Al, Si, K, Ca, Ce, and Nd abundances of 2283 red giant stars in 31 globular clusters from high-resolution spectra observed in both the Northern and Southern hemisphere by the SDSS-IV APOGEE-2 survey. This unprecedented homogeneous data set, largest to date, allows us to discuss the intrinsic Fe spread, the shape, and statistics of Al-Mg and N-C anti-correlations as a function of cluster mass, luminosity, age, and metallicity for all 31 clusters. We find that the Fe spread does not depend on these parameters within our uncertainties including cluster metallicity, contradicting earlier observations. We do not confirm the metallicity variations previously observed in M22 and NGC 1851. Some clusters show a bimodal Al distribution, while others exhibit a continuous distribution as has been previously reported in the literature. We confirm more than two populations in ω Cen and NGC 6752, and find new ones in M79. We discuss the scatter of Al by implementing a correction to the standard chemical evolution of Al in the Milky Way. After correction, its dependence on cluster mass is increased suggesting that the extent of Al enrichment as a function of mass was suppressed before the correction. We observe a turnover in the Mg-Al anticorrelation at very low Mg in ω Cen, similar to the pattern previously reported in M15 and M92. ω Cen may also have a weak K-Mg anticorrelation, and if confirmed, it would be only the third cluster known to show such a pattern.

Key words: astronomical data bases: miscellaneous – surveys – stars, galaxies: abundances – stars: late-type – globular clusters: general – galaxies: fundamental parameters.

1 INTRODUCTION

During most of the 20th century it was believed that globular clusters (GCs) exhibit only one generation of stars. However, detailed photometric and spectroscopic studies of Galactic globular clusters over the past 30 yr have revealed great complexity in the elemental abundances of their stars, from the main sequence through to the asymptotic giant branch (AGB). Most light elements show star-to-star variations in almost all GCs and these large variations are generally interpreted as the result of chemical feedback from an earlier generation of stars (Gratton et al. 2001; Cohen, Briley & Stetson 2002), rather than inhomogeneities in the original stellar

★ E-mail: meszi@gothard.hu
† NSF Astronomy and Astrophysics Postdoctoral Fellow

cloud from which these stars formed. Thus, the current scenario of GC evolution generally assumes that more than one population of stars were formed in each cluster, and the chemical makeup of stars that formed later is polluted by material produced by the first generation.

The origin of the polluting material remains to be established and it has obvious bearings on the time-scales for the formation of the cluster itself and its mass budget. Proposed candidate polluters include intermediate mass stars in their AGB phase (Ventura et al. 2001), fast rotating massive stars losing mass during their main sequence phase (Decressin et al. 2007), novae (Maccarone & Zurek 2012), massive binaries (de Mink et al. 2009), and supermassive stars (Denissenkov et al. 2014). These potential contributions obviously operate on different time-scales and require a different amount of stellar mass in the first generation. In order to constrain these models and to gain an overall understanding of the multiple stellar populations in globular clusters we need comprehensive studies with a relatively complete and unbiased data set. This requires a focused effort by Galactic archaeology surveys to obtain and uniformly analyse spectra for large samples of globular cluster stars across a wide range of metallicity.

There are two main fronts in exploring multiple populations (MPs) in GCs: photometry and spectroscopy. Several larger photometric surveys have been conducted to explore MPs in almost all GCs (e.g. Piotto et al. 2007; Sarajedini et al. 2007; Piotto et al. 2015; Milone et al. 2017; Soto et al. 2017), using the data from the *Hubble Space Telescope* achieving unprecedented photometric precision. Using high-resolution spectroscopy the Lick-Texas group (e.g. Sneden et al. 1991, 1992, 1997, 2004; Kraft et al. 1992, 1995; Sneden, Pilachowski & Kraft 2000; Ivans et al. 2001) conducted the first large survey of northern clusters using three different telescopes and spectrographs. Also using high-resolution spectroscopy Carretta et al. (2009a,b,c) have carried out the first detailed survey of southern clusters with the VLT telescopes, exploring the Na-O and Al-Mg anticorrelations, which are the result of Ne-Na and Mg-Al cycles occurring in the H-burning shell of the first population stars whose nucleosynthetic products were later distributed through the cluster. We refer the reader to Bastian & Lardo (2018) for a complete overview on MPs in GCs.

With the appearance of high spectral resolution sky surveys some of these southern clusters were revisited by the *Gaia*-ESO survey (Gilmore et al. 2012) focusing on the same two element pairs (Pancino et al. 2017). The first homogeneous exploration of 10 northern clusters was carried out by Mészáros et al. (2015), which was updated by Masseron et al. (2019), both using data from the SDSS-III (Eisenstein et al. 2011) Apache Point Observatory Galactic Evolution Experiment (APOGEE) survey. Results for additional clusters observed by APOGEE were published by Schiavon et al. (2017), Tang et al. (2017), and Fernández-Trincado et al. (2019). Its successor, SDSS-IV (Blanton et al. 2017) APOGEE-2 (Majewski et al. 2017) started in the summer of 2014 and ends in 2020, further expanding the number of observed GCs from the Southern hemisphere. Comparison of northern and southern clusters was difficult previously because many observations were carried out with different telescopes and abundance determination techniques that may have systematic errors of their own. The APOGEE survey is the first spectroscopic survey that covers both the northern and southern sky by installing two twin spectrographs, identical in design, on the Sloan 2.5 m telescope (Gunn et al. 2006) at the Apache Point Observatory (APO) and the du Pont 2.5 m telescope at Las Campanas Observatory (LCO). In an effort to create the first truly systematic study of the chemical makeup of multiple populations in all GCs, Masseron et al. (2019) reanalysed the 10 clusters observed from APO (Mészáros et al. 2015) with an updated pipeline.

In this paper we discuss 21 new (mostly southern) clusters observed from both LCO and APO by following the same steps of atmospheric parameter and abundance determination as Masseron et al. (2019) and combine them with the 10 northern clusters discussed by Masseron et al. (2019). Because M12 was observed from both observatories, we use this cluster to check how homogeneous the abundances are from APO and LCO. By combining observations from APO and LCO, we are able to discuss the statistics of Al-Mg and N-C anticorrelations as a function of main cluster parameters in a much larger sample of clusters than was previously possible. Na-O anticorrelation is not included in our study, because Na lines in the *H*-band are too weak to be observable in almost all of our sample of clusters.

There are various labels used in the literature for stars within GCs that are enriched in He, N, Na, Al, and are depleted in O, C, and Mg, such as second-generation stars and chemically enriched stars. We will use the term second-generation/population (SG) stars when referring to stars that have [Al/Fe]>0.3 dex, and first generation/population (FG) when [Al/Fe]<0.3 dex (see Section 5.1). While more than two populations can be identified based on abundances in some clusters, we focus on simplifying the term to refer to all stars that satisfy the above criteria, as second/first-generation/population stars for easier discussion. On the other hand, most metal-rich clusters ([Fe/H]>-1) are enriched in Al ([Al/Fe]>0.3 dex), but appear to host only a single population of stars, so they are chemically enriched but any possible SG stars have the same [Al/Fe] content as FG stars within our errors (see Section 7.3 for more discussion). We treat these clusters as having one FG star group when looking at MPs based on Al abundances.

2 MEMBERSHIP ANALYSIS

Table 1 lists the globular clusters observed by APOGEE-2, along with the main parameters from the Harris catalogue (Harris 1996, 2010 edition), *Gaia* DR2 (Baumgardt et al. 2019), and from Baumgardt & Hilker (2018). A more detailed description of the general target selection of APOGEE and APOGEE-2 can be found in Zasowski et al. (2013, 2017), respectively. Our target selection follows that of Mészáros et al. (2015) and Masseron et al. (2019). We select stars based on their radial velocity first, their distance from cluster centre second, and their metallicity third. In radial velocity, we required stars to be within three times the velocity dispersion of the mean cluster velocity, and in distance we required stars to be within the tidal radius. The metallicity cut was usually set to ±0.5 dex around the cluster average, except for clusters with suspected intrinsic Fe spread for which the metallicity cut was skipped, or only obvious field stars were deleted (for example, stars with solar-like metallicity in otherwise metal-poor clusters). For this paper we made important updates by selecting the average cluster radial velocity and its scatter from *Gaia* DR2 (Baumgardt & Hilker 2018) rather than from Harris (1996, 2010 edition). In addition, we introduced a fourth step that is based upon selecting stars that have proper motion within a 1.5–2.5 mas yr^{-1} range (depending on the cluster) around the cluster average proper motion from the *Gaia* DR2 catalogue (Gaia Collaboration 2018).

These two improvements were not adopted by Masseron et al. (2019), but now we refine the list of stars presented in that study. While the selected members of those 10 northern clusters have only changed slightly, because some stars were added or deleted, we did not re-derive atmospheric parameters and abundances for stars that

Table 1. Properties of clusters from the literature.

ID	Name	N_1 [a] All	N_2 [b] S/N > 70	[Fe/H]	$E(B-V)$	R_t '	V_{disp} km s^{-1}	RA	Dec	V_{helio} km s^{-1}	$\mu_{\alpha*}$ mas yr^{-1}	μ_δ mas yr^{-1}
NGC 104	47 Tuc	186	151	− 0.72	0.04	42.9	12.2	00 24 05.67	− 72 04 52.6	− 17.2	5.25	− 2.53
NGC 288		43	40	− 1.32	0.03	12.9	3.3	00 52 45.24	− 26 34 57.4	− 44.8	4.22	− 5.65
NGC 362		56	40	− 1.26	0.05	16.1	8.8	01 03 14.26	− 70 50 55.6	223.5	6.71	− 2.51
NGC 1851		43	30	− 1.18	0.02	11.7	10.2	05 14 06.76	− 40 02 47.6	320.2	2.12	− 0.63
NGC 1904	M79	26	25	− 1.60	0.01	8.3	6.5	05 24 11.09	− 24 31 29.0	205.6	2.47	− 1.59
NGC 2808		77	71	− 1.14	0.22	15.6	14.4	09 12 03.10	− 64 51 48.6	103.7	1.02	0.28
NGC 3201		179	152	− 1.59	0.24	28.5	5.0	10 17 36.82	− 46 24 44.9	494.3	8.35	− 2.00
NGC 4147		3	1	− 1.80	0.02	6.3	3.1	12 10 06.30	+18 32 33.5	179.1	− 1.71	− 2.10
NGC 4590	M68	37	36	− 2.23	0.05	13.7	3.7	12 39 27.98	− 26 44 38.6	− 93.2	− 2.75	1.78
NGC 5024	M53	41	39	− 2.10	0.02	30.3	5.9	13 12 55.25	+18 10 05.4	− 63.1	− 0.11	− 1.35
NGC 5053		17	17	− 2.27	0.01	11.8	1.6	13 16 27.09	+17 42 00.9	42.5	− 0.37	− 1.26
NGC 5139	ω Cen	898	775	− 1.53	0.12	57.0	17.6	13 26 47.24	− 47 28 46.5	232.7	− 3.24	− 6.73
NGC 5272	M3	153	148	− 1.50	0.01	38.2	8.1	13 42 11.62	+28 22 38.2	− 147.2	− 0.14	− 2.64
NGC 5466		15	7	− 1.98	0.00	34.2	1.6	14 05 27.29	+28 32 04.0	106.9	− 5.41	− 0.79
NGC 5634		2	0	− 1.88	0.05	8.4	5.3	14 29 37.30	− 05 58 35.0	− 16.2	− 1.67	− 1.55
NGC 5904	M5	207	191	− 1.29	0.03	28.4	7.7	15 18 33.22	+02 04 51.7	53.8	4.06	− 9.89
NGC 6121	M4	158	153	− 1.16	0.35	32.5	4.6	16 23 35.22	− 26 31 32.7	71.0	− 12.48	− 18.99
NGC 6171	M107	66	55	− 1.02	0.33	17.4	4.3	16 32 31.86	− 13 03 13.6	− 34.7	− 1.93	− 5.98
NGC 6205	M13	127	103	− 1.53	0.02	25.2	9.2	16 41 41.24	+36 27 35.5	− 244.4	− 3.18	− 2.56
NGC 6218	M12	86	54	− 1.37	0.19	17.6	4.5	16 47 14.18	− 01 56 54.7	− 41.2	− 0.15	− 6.77
NGC 6229		7	5	− 1.47	0.01	10.0	7.1	16 46 58.79	+47 31 39.9	− 138.3	− 1.19	− 0.46
NGC 6254	M10	87	84	− 1.56	0.28	21.5	6.2	16 57 09.05	− 04 06 01.1	74.0	− 4.72	− 6.54
NGC 6316		1	1	− 0.45	0.54	5.9	9.0	17 16 37.30	− 28 08 24.4	99.1	− 4.97	− 4.61
NGC 6341	M92	70	67	− 2.31	0.02	15.2	8.0	17 17 07.39	+43 08 09.4	− 120.7	− 4.93	− 0.57
NGC 6388		26	9	− 0.55	0.37	6.2	18.2	17 36 17.23	− 44 44 07.8	83.4	− 1.33	− 2.68
NGC 6397		158	141	− 2.02	0.18	15.8	5.2	17 40 42.09	− 53 40 27.6	18.4	3.30	− 17.60
NGC 6441		17	5	− 0.46	0.47	8.0	18.8	17 50 13.06	− 37 03 05.2	17.1	− 2.51	− 5.32
NGC 6522		7	5	− 1.34	0.48	16.4	8.2	18 03 34.02	− 30 02 02.3	− 14.0	2.62	− 6.40
NGC 6528		2	1	− 0.11	0.54	16.6	6.4	18 04 49.64	− 30 03 22.6	211.0	− 2.17	− 5.52
NGC 6539		1	1	− 0.63	1.02	21.5	5.9	18 04 49.68	− 07 35 09.1	35.6	− 6.82	− 3.48
NGC 6544		7	7	− 1.40	0.76	2.05	6.4	18 07 20.58	− 24 59 50.4	− 36.4	− 2.34	− 18.66
NGC 6553		8	7	− 0.18	0.63	8.2	8.5	18 09 17.60	− 25 54 31.3	0.5	0.30	− 0.41
NGC 6656	M22	80	20	− 1.70	0.34	29.0	8.4	18 36 23.94	− 23 54 17.1	− 147.8	9.82	− 5.54
NGC 6715	M54	22	7	− 1.49	0.15	10.0	16.2	18 55 03.33	− 30 28 47.5	142.3	− 2.73	− 1.38
NGC 6752		153	138	− 1.54	0.04	55.3	8.3	19 10 52.11	− 59 59 04.4	− 26.2	− 3.17	− 4.01
NGC 6760		3	3	− 0.40	0.77	7.2	···	19 11 12.01	+01 01 49.7	− 1.6	− 1.11	− 3.59
NGC 6809	M55	96	92	− 1.94	0.08	16.3	4.8	19 39 59.71	− 30 57 53.1	174.8	− 3.41	− 9.27
NGC 6838	M71	39	35	− 0.78	0.25	9.0	3.3	19 53 46.49	+18 46 45.1	− 22.5	− 3.41	− 2.61
NGC 7078	M15	133	104	− 2.37	0.10	21.5	12.9	21 29 58.33	+12 10 01.2	− 106.5	− 0.63	− 3.80
NGC 7089	M2	26	24	− 1.65	0.06	21.5	10.6	21 33 27.02	− 00 49 23.7	− 3.6	3.51	− 2.16
Pal 5		5	5	− 1.41	0.03	16.3	0.6	15 16 05.25	− 00 06 41.8	− 58.4	− 2.77	− 2.67
Pal 6		5	4	− 0.91	1.46	8.4	···	17 43 42.20	− 26 13 21.0	181.0	− 9.17	− 5.26
Terzan 5		7	7	− 0.23	2.28	13.3	19.0	17 48 04.80	− 24 46 45.0	− 82.3	− 1.71	− 4.64
Terzan 12		1	1	− 0.50	2.06	···	···	18 12 15.80	− 22 44 31.0	94.1	− 6.07	− 2.63

Notes. Average metallicities, reddenings, tidal radii, and coordinates were taken from Harris (1996, 2010 edition). Radial and dispersion velocities are from Baumgardt & Hilker (2018). Proper motions were taken from Baumgardt et al. (2019).
[a]The number of all stars in our sample.
[b]The number of stars with S/N > 70.

Table 2. Atmospheric parameters and abundances of individual stars.

2MASS ID	Cluster	Status	T_{eff}	log g	[Fe/H]	$\sigma_{[Fe/H]}$	[C/Fe]	limit[a]	$\sigma_{[C/Fe]}$	N_C	[N/Fe]	...
2M13121714+1814178	M53	RGB	4574	0.87	−2.007	0.121	···	0	···	0	···	
2M13122857+1815051	M53	RGB	4202	− 0.07	−1.982	0.088	···	0	···	0	0.834	
2M13123506+1814286	M53	RGB	4639	1.02	−1.894	0.124	···	0	···	0	···	
2M13123617+1807320	M53	RGB	4514	0.74	−1.841	0.083	···	0	···	0	···	
2M13123617+1827323	M53	RGB	4652	1.05	−1.928	0.119	···	0	···	0	···	

Notes. This table is available in its entirety in machine-readable form in the online journal. A portion is shown here, with reduced number of columns, for guidance regarding its form and content. Star identification from Carretta et al. (2009b) was added in the last column.
[a]The number of lines used in the abundances analysis from BACCHUS (Masseron, Merle & Hawkins 2016).

Table 3. Abundance averages and scatter.

ID	Name	[Fe/H] Carretta	[Fe/H] Pancino	Mass 10^3 $M_\odot$	V_{ABS}	Age	[Fe/H] Average	[Fe/H] Scatter	[Fe/H]^a Error	[Al/Fe] Average	[Al/Fe] Scatter
NGC 104	47 Tuc	−0.768	−0.71	779	−9.42	12.8	−0.626	0.107	0.082	0.583	0.129
NGC 288		−1.305	···	116	−6.75	12.2	−1.184	0.114	0.059	0.368	0.175
NGC 362		···	−1.12	345	−8.43	10.0	−1.025	0.080	0.056	0.241	0.240
NGC 1851		···	−1.07	302	−8.33	···	−1.033	0.082	0.077	0.192	0.251
NGC 1904	M79	−1.579	−1.51	169	−7.86	12.0	−1.468	0.092	0.062	0.449	0.530
NGC 2808		−1.151	−1.03	742	−9.39	11.2	−0.925	0.101	0.070	0.328	0.446
NGC 3201		−1.512	···	149	−7.45	11.1	−1.241	0.102	0.061	0.099	0.345
NGC 4590	M68	−2.265	···	123	−7.37	12.7	−2.161	0.100	0.108	0.302	0.419
NGC 5024	M53	···	···	380	−8.71	12.7	−1.888	0.101	0.108	0.346	0.507
NGC 5053		···	···	56.6	−6.76	12.3	−2.057	0.095	0.108	0.397	0.447
NGC 5139	ω Cen	···	···	3550	−10.26	···	−1.511	0.205	0.077	0.586	0.533
NGC 5272	M3	···	···	394	−8.88	11.4	−1.388	0.127	0.068	0.249	0.425
NGC 5466		···	···	45.6	−6.98	13.6	−1.827	0.070	0.105	0.246	0.663
NGC 5904	M5	−1.340	···	372	−8.81	11.5	−1.178	0.102	0.062	0.297	0.346
NGC 6121	M4	−1.168	···	96.9	−7.19	13.1	−1.020	0.086	0.042	0.708	0.121
NGC 6171	M107	−1.033	···	87	−7.12	13.4	−0.852	0.106	0.076	0.538	0.118
NGC 6205	M13	···	···	453	−8.55	11.7	−1.432	0.129	0.078	0.536	0.517
NGC 6218	M12	−1.310	···	86.5	−7.31	13.4	−1.169	0.094	0.073	0.279	0.164
NGC 6229		···	···	291	−8.06	···	−1.214	0.127	0.038	0.189	0.276
NGC 6254	M10	−1.575	···	184	−7.48	12.4	−1.345	0.102	0.074	0.451	0.549
NGC 6341	M92	···	···	268	−8.21	13.2	−2.227	0.096	0.133	0.562	0.414
NGC 6388		−0.441	···	1060	−9.41	11.7	−0.438	0.074	0.152	0.341	0.078
NGC 6397		−1.988	···	88.9	−6.64	13.4	−1.887	0.092	0.088	0.451	0.408
NGC 6656	M22	···	···	416	−8.50	12.7	−1.524	0.112	0.092	0.461	0.407
NGC 6715	M54	···	···	1410	−9.98	10.8	−1.353	0.039	0.059	0.189	0.499
NGC 6752		−1.555	−1.48	239	−7.73	13.8	−1.458	0.076	0.052	0.634	0.455
NGC 6809	M55	−1.934	···	188	−7.57	13.8	−1.757	0.080	0.067	0.358	0.454
NGC 6838	M71	−0.832	···	49.1	−5.61	12.7	−0.530	0.112	0.088	0.463	0.099
NGC 7078	M15	−2.320	···	453	−9.19	13.6	−2.218	0.121	0.136	0.438	0.446
NGC 7089	M2	···	−1.47	582	−9.03	11.8	−1.402	0.069	0.055	0.400	0.464
Pal 5		···	···	13.9	−5.17	···	−1.214	0.085	0.073	0.053	0.130

		[Al/Fe] Average >0.3dex	[Al/Fe] Average <0.3dex	[Al/Fe] Scatter >0.3dex	$f_{enriched}$	S1^b Average	S1^b Scatter	[N/Fe] Average	[N/Fe] Scatter	S2^c Average	S2^c Scatter
NGC 104	47 Tuc	0.586	···	0.128	···	0.779	0.074	0.924	0.407	1.918	0.112
NGC 288		0.462	0.175	0.121	···	0.804	0.054	0.832	0.341	1.919	0.107
NGC 362		0.468	0.049	0.125	···	0.600	0.050	1.038	0.360	1.738	0.112
NGC 1851		0.495	0.033	0.095	···	0.637	0.056	1.034	0.355	1.706	0.128
NGC 1904	M79	0.826	−0.136	0.288	0.609	0.634	0.029	···	···	···	···
NGC 2808		0.802	0.025	0.341	0.391	0.589	0.056	0.937	0.440	1.759	0.120
NGC 3201		0.635	−0.081	0.198	0.252	0.607	0.053	0.789	0.351	1.802	0.069
NGC 4590	M68	0.648	−0.111	0.207	0.545	0.709	0.093	···	···	···	···
NGC 5024	M53	0.917	−0.061	0.182	0.417	0.830	0.101	···	···	···	···
NGC 5053		0.772	−0.029	0.208	···	0.656	0.127	···	···	···	···
NGC 5139	ω Cen	0.935	0.058	0.389	0.603	0.799	0.096	1.273	0.452	2.074	0.177
NGC 5272	M3	0.809	−0.027	0.203	0.331	0.689	0.083	0.861	0.297	1.805	0.187
NGC 5466		···	−0.161	···	···	0.644	0.058	···	···	···	···
NGC 5904	M5	0.604	0.010	0.196	0.484	0.693	0.078	1.094	0.393	1.791	0.154
NGC 6121	M4	0.709	···	0.121	···	0.875	0.064	0.894	0.269	1.808	0.086
NGC 6171	M107	0.538	···	0.118	···	0.815	0.087	0.911	0.468	2.032	0.123
NGC 6205	M13	0.860	−0.050	0.325	0.644	0.754	0.097	1.248	0.268	1.903	0.116
NGC 6218	M12	0.444	0.154	0.088	···	0.759	0.064	1.028	0.347	1.980	0.089
NGC 6229		···	0.057	···	···	0.669	0.056	0.571	0.052	···	···
NGC 6254	M10	0.981	−0.039	0.265	0.481	0.703	0.066	1.136	0.291	1.944	0.096
NGC 6341	M92	0.770	−0.092	0.197	0.759	0.825	0.087	···	···	···	···
NGC 6388		0.381	···	0.045	···	0.544	0.088	1.020	0.323	1.773	0.098
NGC 6397		0.701	−0.094	0.177	0.686	0.724	0.092	···	···	···	···
NGC 6656	M22	0.662	−0.100	0.248	···	0.692	0.111	···	···	···	···
NGC 6715	M54	···	−0.072	···	···	0.629	0.025	···	···	···	···
NGC 6752		0.832	0.004	0.326	0.761	0.751	0.053	1.054	0.197	1.812	0.106
NGC 6809	M55	0.734	−0.066	0.249	0.531	0.764	0.051	1.093	0.102	···	···
NGC 6838	M71	0.477	···	0.088	···	0.704	0.080	0.992	0.441	2.093	0.113

Table 3 – *continued*

ID	Name	[Fe/H] Carretta	[Fe/H] Pancino	Mass 10^3 $M_\odot$	V_{ABS}	Age	[Fe/H] Average	[Fe/H] Scatter	[Fe/H]^a Error	[Al/Fe] Average	[Al/Fe] Scatter
NGC 7078	M15	0.752	−0.056	0.231	0.613	0.803	0.097	...	...	...	...
NGC 7089	M2	0.785	−0.061	0.212	0.545	0.699	0.048	1.058	0.132	1.845	0.154
Pal 5		...	−0.009	...	...	0.615	0.044	0.699	0.224	1.785	0.087

Notes. This table lists statistics for 31 GCs remaining after our refining procedure described in Section 2 and 3.1. Scatter is defined as the standard deviation around the mean. Masses are taken from Baumgardt & Hilker (2018), and we use the ages compiled by Krause et al. (2016).
[a]The error of [Fe/H] is the average uncertainty for a given cluster.
[b][(Mg+Al+Si)/Fe].
[c][(C+N+O)/Fe].

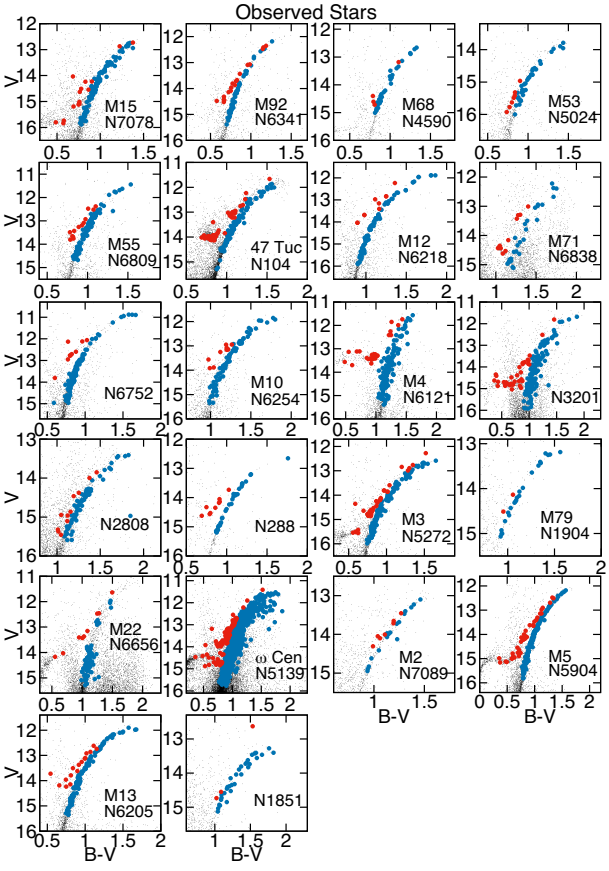

Figure 1. The CMD of observed stars by APOGEE in 22 clusters in common with Stetson et al. (2019). AGB/HB stars are denoted by red dots, the RGB stars are by blue dots.

remained members, as our analysis method has not changed. It is important to note that only a couple of stars have been deleted from these GCs, and the main science results and conclusions presented in Masseron et al. (2019) remain the same. However, all figures, including data for those 10 clusters have been updated for this paper.

The individual atmospheric parameters and the derived abundances are listed in Table 2, while the abundance averages and RMS scatters for each cluster are presented in Table 3. Table 2 contains results for all stars and clusters that were analysed, altogether 3382 stars in 44 clusters. However, we do not discuss all clusters and stars. We make a quality selection according to the following criteria. High S/N spectra are essential to determine abundances from atomic and molecular features. Most of the tests done by the APOGEE team concluded that abundances become reliable around S/N = 70–100, however, objects with poorer S/N have also been analysed and included in Table 2. The spectra have been processed by the APOGEE data processing pipeline (Nidever et al. 2015). Another criterion was that a cluster has to have at least five members with S/N > 70 to qualify for further analysis. The following clusters did not meet this criterion: NGC 4147, NGC 5634, NGC 6316, NGC 6528, NGC 6539, NGC 6760, Pal 6, and Terzan 12. While we do not use these clusters in our analysis, their abundances and atmospheric parameters were derived and listed in Table 2 for reference. The remaining 36 clusters were further refined based on their reddening values as described in the next section. Table 3 contains the clusters remaining after our refining procedure.

3 ATMOSPHERIC PARAMETERS AND ABUNDANCES

3.1 BACCHUS description

Since the method of deriving atmospheric parameters and abundances is identical to that of Masseron et al. (2019), we only give a short overview of it in this paper. We use the Brussels Automatic Code for Characterizing High accUracy Spectra (BACCHUS) (Masseron et al. 2016) to determine the metallicity and abundances, but not effective temperatures and surface gravities. Microturbulent velocities were computed from the surface gravities using the following equation:

$$v_{\rm micro} = 2.488 - 0.8665 \cdot \log g + 0.1567 \cdot \log g \cdot \log g.$$

This relation was originally determined from the *Gaia*-ESO survey by cancelling the trend of abundances against equivalent widths of selected Fe I lines (Masseron et al. 2019). The validity of this relation in the *H*-band was checked by Masseron et al. (2019). Due to problems with ASPCAP (García Pérez et al. 2014) effective temperatures at low metallicities, [M/H]<−0.7 dex (detailed by Mészáros et al. 2015; Jönsson et al. 2018; Masseron et al. 2019; Nataf et al. 2019; Nidever et al. 2019), these were computed from 2MASS colours using the equations from González Hernández & Bonifacio (2009). Surface gravities were derived from isochrones (Bertelli et al. 2008, 2009; Marigo et al. 2017) by taking into account their evolutionary state. The log g was determined by taking the photometric effective temperature and reading the log g, by interpolating through surface gravities, corresponding to that effective temperature from the isochrone. AGB and RGB stars were selected by combining our list of stars with the ground-based photometric catalogue compiled by Stetson et al. (2019) for 22 clusters in common with our sample. Our selection was based on the star's position on the V−(B−V) colour–magnitude diagram (see e.g. García-Hernández et al. 2015) shown in Fig. 1. For clusters not

Table 4. Overview of homogeneous spectroscopic surveys of globular clusters.

Reference	N_{stars}	N_{cl}	Element pairs[a]	Observatory[b]	Survey	Comments
Carretta et al. (2009a,b,c)	1958	19	Na-O, Al-Mg	ESO/VLT	Carretta	UVES/Giraffe combined.
Mészáros et al. (2015)	428	10	Al-Mg, N-C	APO	APOGEE	–
Pancino et al. (2017)	572	9	Al-Mg	ESO/VLT	*Gaia*-ESO	–
Masseron et al. (2019)	885	10	Al-Mg, N-C	APO	APOGEE	Same clusters as Mészáros et al. (2015).
Nataf et al. (2019)	1581	25	Al-Mg, N-C	APO/LCO	APOGEE	Payne analysis only.
This paper	2283	31	Al-Mg, N-C	APO/LCO	APOGEE	Includes data from Masseron et al. (2019).

Notes. Clusters with less than five observed members were excluded from the statistics.
[a]The main element pairs used to study multiple populations.
[b]ESO/VLT: Very large telescope at the European Southern Observatory, APO: Apache Point Observatory, LCO: Las Campanas Observatory.

Table 5. Selected parameter cuts for analysis.

Abundance	T_{eff} K	[Fe/H] dex	$\sigma_{[X/Fe]}$ dex
[C/Fe]	<4600	>−1.9	<0.2
[N/Fe]	<4600	>−1.9	<0.2
[O/Fe]	<4600	>−1.9	<0.2
[Mg/Fe]	<5500	>−2.5	<0.2
[Al/Fe]	<5500	>−2.5	<0.2
[Si/Fe]	<5500	>−2.5	<0.2
[K/Fe]	<4600	>−1.5	<0.2
[Ca/Fe]	<5500	>−2.5	<0.2
[Fe/H]	<5500	>−2.5	<0.2
[Ce/Fe]	<4400	>−1.8	<0.2
[Nd/Fe]	<4400	>−1.8	<0.2

Notes. A S/N > 70 cut is also applied. All averages and scatter values were computed using stars that satisfy these conditions including the figures shown in the paper.

listed in the Stetson catalogue we assumed all stars to be on the RGB. For further information on our abundance determination methods, comparisons to ASPCAP, and their accuracy and precision (generally below 0.1 dex) we refer the reader to Section 3 of Masseron et al. (2019). The absorption lines selected for abundance determination are the same as those used by Masseron et al. (2019). Random errors were derived from the line-by-line abundance dispersion.

The use of photometric temperatures introduces its own set of problems mostly related to high $E(B-V)$ values. The González Hernández & Bonifacio (2009) relations are very sensitive to small changes in $E(B-V)$, which is very important in high reddening clusters that may in addition suffer from significant differential reddening inside the cluster. For this reason the list of clusters was further limited by removing clusters with $E(B-V) > 0.4$ according to the Harris catalogue. Our metallicities derived from highly reddened spectra are also significantly larger than what the optical studies have found making us believe that either reddening and/or photometric temperatures are not reliable when $E(B-V) > 0.4$. This issue is explored in more detail in Section 4.1. The following five clusters have at least five members with S/N > 70, but have $E(B-V) > 0.4$: NGC 6441, NGC 6522, NGC 6544, NGC 6553, and Terzan 5. The final sample after the S/N and reddening cuts includes 2283 stars in 31 clusters, and we use this sample to study statistics of Mg-Al and N-C anticorrelations throughout the paper. Previous homogeneous surveys are listed in Table 4 for easy comparison.

While Table 2 lists all abundances we were able to measure regardless of S/N, we introduced the previously mentioned S/N > 70 cut in all figures and statistics. Upper limits are also listed in

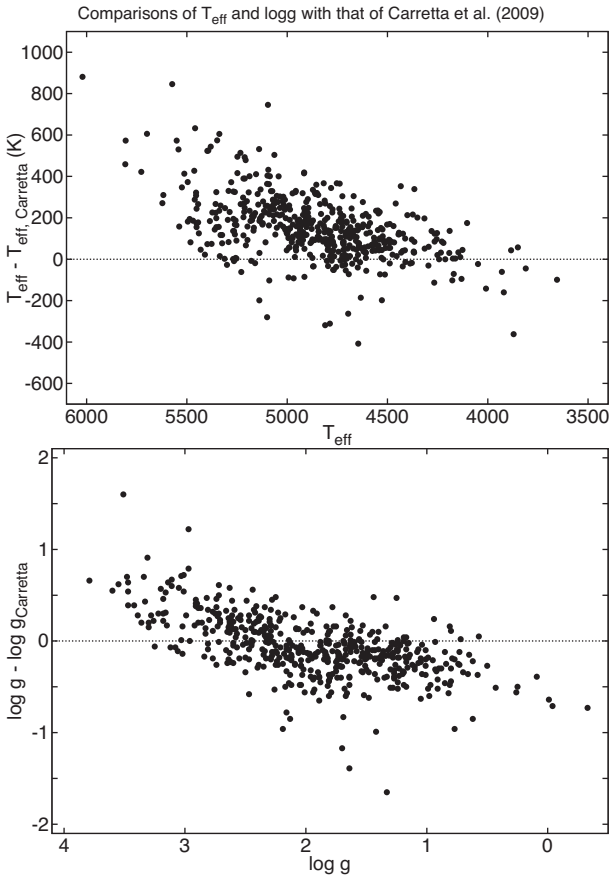

Figure 2. Top panel: Comparisons of our T_{eff} scale from González Hernández & Bonifacio (2009) with Carretta et al. (2009a,b,c), who used Alonso, Arribas & Martinez-Roger (1999, 2001). Bottom panel: Comparisons of our surface gravities with the same source.

Table 2, but not plotted in any of the figures, or included when calculating cluster averages and scatters, because we made the decision to study the behaviour of anticorrelations based on only real measurements. We implemented a maximum temperature cut of 4600 K for CNO and K, because for higher temperatures the molecular (atomic in case of K) lines become too weak, rendering abundances of these elements unreliable. We use 5500 K for the rest of the elements as maximum temperature above which errors start to significantly increase. Stars plotted in all figures in Sections 4 to 8 have elemental abundances with internal errors smaller than 0.2 dex to reduce contamination from highly unreliable measurements. Stars with abundances outside these parameter regions are published in Table 2, but we caution the reader to carefully examine these

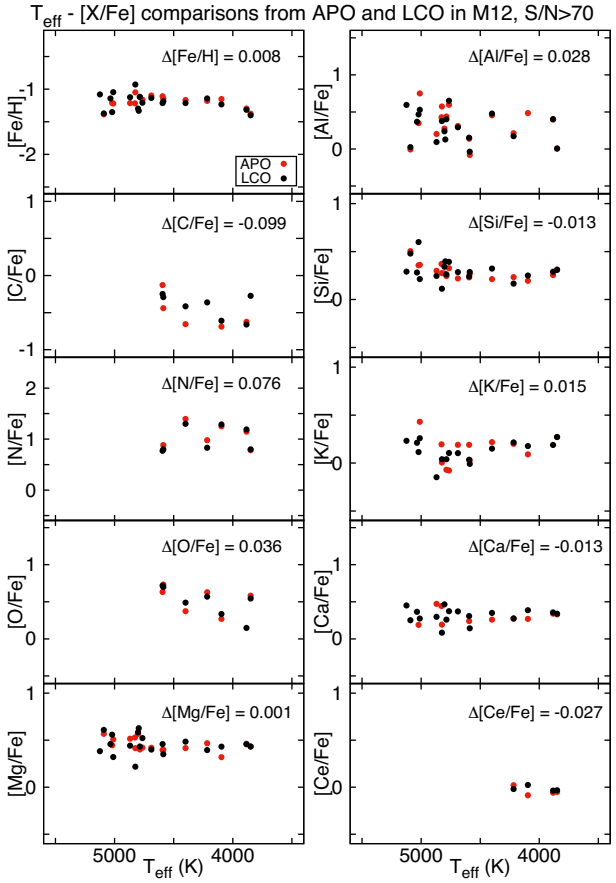

Figure 3. Comparison of stars observed from both APO (red dots) and LCO (black dots) in M12. The differences between APO and LCO printed in each panel are on the level or smaller than the average internal error of each element.

values before drawing scientific conclusions. These limitations were set in place when calculating abundance averages and scatter for all clusters and are listed in Table 5. The error in the mean [Fe/H] is smaller than the dot used to represent the data in all figures, thus errorbars were not plotted in any of the figures. For the abundance−abundance plots we only highlighted the average error of each abundance for simplicity, but Table 2 lists all individual errors.

3.2 Comparisons of $T_{\rm eff}$ and log g values with the literature

We limit our discussion of comparisons of $T_{\rm eff}$ and log g with literature to that of Carretta et al. (2009a,b,c), since that is the literature source we have the most stars in common with, 514 altogether, out of the list of papers in Table 4. Star identification from Carretta et al. (2009b) was added to Table 2 for easy comparison.

The difference between our parameters and those of Carretta et al. (2009a,b,c) can be seen in Fig. 2. The systematic offset seen between the two temperatures are the characteristics of the photometric temperature conversions (and differences in colours used to calculate the temperature) of González Hernández & Bonifacio (2009) and Alonso et al. (1999, 2001), which was used by Carretta et al. (2009a,b,c). The temperature difference is generally between ±300 K, but it increases with increasing temperature.

Similar structure can be seen when comparing surface gravities, because the temperature and log g have a simple linear correlation on the RGB, so any systematic difference seen in the temperature scale will propagate to log g. These discrepancies may also propagate to metallicity, further discussed in Section 4.1, and/or individual abundances, which is expected when temperature scales differ from one another.

3.3 Comparisons of APO and LCO observations

As mentioned at the end of the introduction, APOGEE-2 uses two spectrographs identical in design at two observatories, APO and LCO to map all parts of the Milky Way. The identical design makes it possible to directly derive atmospheric parameters and abundances that are believed to be on the same scale by observing the same stars from both observatories. The observing strategy is carefully planned (Zasowski et al. 2017) to observe stars with both telescopes that cover the full parameter range ASPCAP operates in so that any differences between the final results can be carefully studied and calibrated if necessary. In terms of globular clusters, there is only one that has been observed with both the northern and southern telescopes: M12, which limits our comparisons to a small range in metallicity.

Fig. 3 shows the BACCHUS derived abundances as a function of effective temperature of the 21 stars in M12 that were both observed from APO and LCO. The difference is calculated for each star that was observed with both telescopes and then averaged together over all the stars. The differences between the two sets of observations range between 0.001 dex for [Mg/Fe] to 0.099 dex for [C/Fe], all of which can be considered as a very good agreement. The discrepancy for C, N, and O are generally larger than for the rest of elements, which is understandable considering that it is more difficult to fit these molecular lines than simple unblended atomic absorption lines. All the differences are on par or smaller than the average error in M12, and thus we conclude that observations from APO and LCO can be directly compared to each other without worrying about any possible large systematic errors. While this test is limited to a unique metallicity ([Fe/H] = −1.2), similar tests on much lager samples of APO-LCO overlapping stars have been done on the ASPCAP analysis of the DR16 data, suggesting that the data from APO and LCO indeed are of similar quality and yield very similar stellar parameters and abundances (Jönsson et al. in preparation).

4 THE FE SCALE

The amount of iron observed in GCs allows the investigation of the history of stars and intracluster medium from which the GCs have formed, because Fe is mostly the result of core–collapse supernovae of high and intermediate mass stars. Additionally, Fe is traditionally used as the tracer of metallicity – the overall abundance of metals in a star. Abundances of iron from homogeneous high-resolution spectroscopic studies are also used to calibrate low-resolution spectroscopic and photometric indices. Setting a true and absolute Fe scale is, thus, one of the most important goals of high-resolution abundance analysis.

4.1 Comparisons with literature

We compare our metallicity scale with those of the Harris catalogue, Carretta et al. (2009c), and *Gaia*-ESO (Pancino et al. 2017). The Harris catalogue is a compilation of various literature sources and all our clusters were selected from it. The largest homogeneous study of iron abundances from high-resolution spectra was previously carried out by Carretta et al. (2009c), 17 of their clusters are in

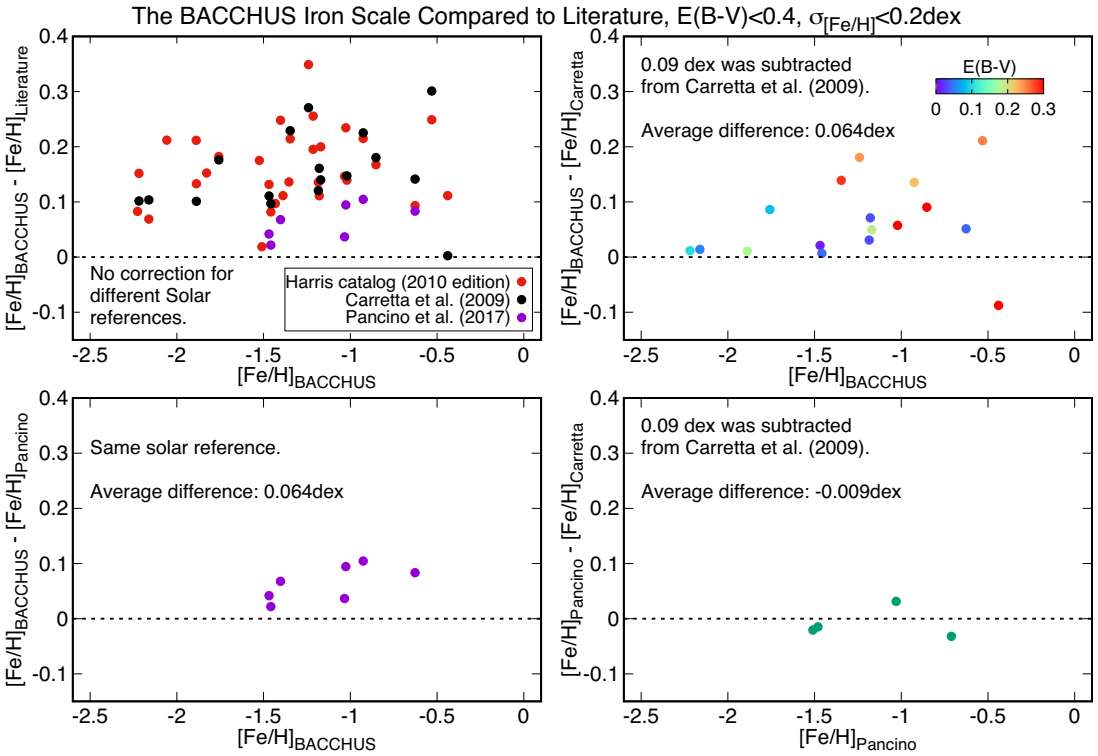

Figure 4. Comparison of mean [Fe/H] cluster values from various literature sources. Differences in the solar reference Fe abundances was corrected where indicated. The three different Fe scales agree roughly within ±0.1 dex after correction.

common with our sample, and we have seven clusters that were also observed by *Gaia*-ESO. We show the four different iron scales on the top left-hand panel of Fig. 4. We find that the [Fe/H] metallicities we derive are on average 0.162 dex higher than those from the Harris catalogue, 0.154 dex higher than Carretta et al. (2009c), 0.064 dex higher than Pancino et al. (2017).

These metallicity differences of GCs have been present in the APOGEE data since the very first data release (Mészáros et al. 2013) and remained in place in all subsequent data releases (Holtzman, Shetrone & Johnson 2015; Holtzman, Hasselquist & Shetrone 2018; Jönsson et al. 2018). This was verified by Mészáros et al. (2015) and by Masseron et al. (2019) using the APOGEE line list, but effective temperatures and surface gravities independent of ASPCAP. Interestingly, Pancino et al. (2017) have also found a similar, although slightly smaller, 0.08 dex higher metallicities than Carretta et al. (2009c) in the seven clusters in common with our sample. This latter study was carried out by the *Gaia*-ESO survey, completely independent of APOGEE observations and using optical spectra instead of the *H*-band. We speculate that the nature of these discrepancies between the three different studies can be attributed to three main factors:

(1) Most of the differences can be explained by the choice of the reference solar abundance table. Carretta et al. (2009c) and some of the compilation found in the Harris catalogue used the Fe reference value of $A(Fe)_{\odot} = 7.54$ derived by Gratton et al. (2003), while Pancino et al. (2017) and APOGEE use 7.45 from Grevesse, Asplund & Sauval (2007). The difference of 0.081 dex between Pancino et al. (2017) and Carretta et al. (2009c) is on the level of the change coming from the different solar Fe references. After applying a correction to account for the different solar reference values, the Pancino et al. (2017) results become almost identical (difference is − 0.009 dex on average) to the Carretta et al. (2009c) results (bottom right-hand panel in Fig. 4). An important aspect of the Pancino et al. (2017) study is that it used spectroscopic temperatures directly derived from the VLT spectra, while Carretta et al. (2009c) used the Alonso et al. (1999, 2001) conversions. The difference between our study and that of Carretta et al. (2009c) reduces to 0.064 dex on average, with a dispersion of 0.073 dex, which is not too different from the statistical uncertainties given by Carretta et al. (2009c).

(2) A separate comparison to Carretta et al. (2009c) is shown on the upper right-hand panel of Fig. 4 after both metallicities are converted to the same scale by subtracting 0.09 dex from Carretta et al. (2009c). A slight correlation can be seen between these two homogeneous studies that is dependent on the $E(B - V)$ value of each cluster. For most of the clusters with $E(B - V) > 0.2$ (NGC 2808, NGC 3201, M10, and M71), we find higher metallicities than for clusters with low reddening, which are still slightly more metal-rich than Carretta et al. (2009c). While one cluster with high reddening, M4, have an average metallicity closer to that of Carretta et al. (2009c) after the correction, we believe that either the photometric calibration does not work at high reddening, the reddening of these clusters is not correct, or this is the result of a systematic difference in the temperature scales of González Hernández & Bonifacio (2009) and that of Alonso et al. (1999, 2001), or a combination of any of these. Generally, these photometric temperature conversions are very sensitive to the reddening, so a small error in the $E(B - V)$ can lead to a large change in temperature, perhaps pushing M4 closer to Carretta et al. (2009c). Also, considering that small errors of $E(B - V)$ may result in large errors in temperature, and high reddening clusters may have

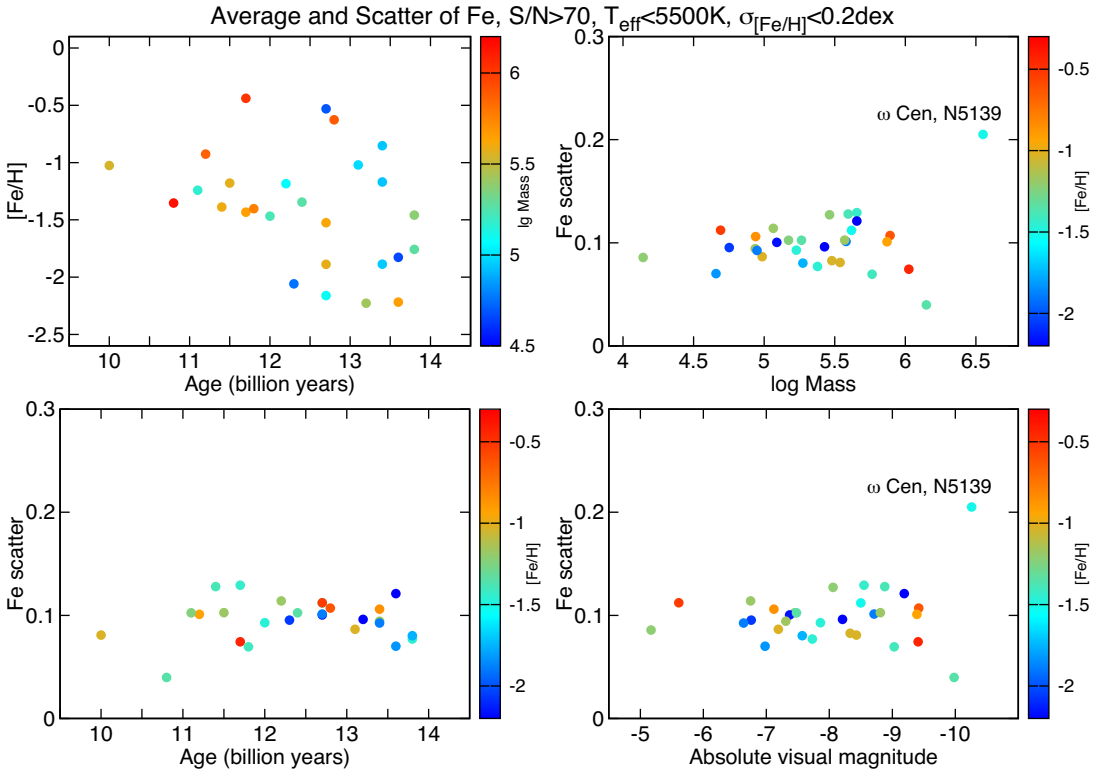

Figure 5. The age–metallicity relation and spread of Fe as a function of cluster properties. No significant correlation is observed with mass, V_{Abs}, and age. ω Cen is the only cluster with significant Fe variations from our sample.

significant differential reddening, we exclude the five clusters with $E(B-V) > 0.4$ listed in Section 3.1 from our study.

(3) An important source of systematic error can be seen in the bottom left-hand panel of Fig. 4, when comparing our metallicities with those of Pancino et al. (2017). This discrepancy is similar to what can be seen in the top right panel when comparing the low-reddening clusters with Carretta et al. (2009c). In this case, all the clusters in common have low reddenings, thus errors from the wrong estimate of $E(B-V)$, or a possible error of the González Hernández & Bonifacio (2009) conversion at high reddenings is minimal. This offset could also be due to how differences in spectroscopic temperature from *Gaia*-ESO and photometric ones from González Hernández & Bonifacio (2009) affect the metallicities. Another possibility is that this 0.064 dex constant offset is the result of NLTE and/or 3D effects which are currently not modelled when fitting the APOGEE (Masseron et al. 2019) or the *Gaia*-ESO spectra.

While our sample is larger than that of Carretta et al. (2009c) and it naturally gives the opportunity to update the iron scale, the choice to do so is tainted by the fact that three independent survey analysis only agree within roughly ± 0.2 dex across the clusters in common. Also, different photometric temperatures from González Hernández & Bonifacio (2009) and from Alonso et al. (1999, 2001) might also introduce a systematic offset when the reddening is too high, possibly both affecting Carretta et al. (2009c) and the results presented in this paper. On top of this, we suspect that a combination of NLTE and 3D effects introduce another systematic offset compared to optical studies. As of writing this paper, NLTE/3D corrections of iron lines are not available for the *H*-band, and any future study using APOGEE data when updating the cosmic iron scale from that of Carretta et al. (2009c) must account for NLTE (and/or 3D) effects of iron lines, which may be as high as 0.06 dex (Masseron et al. 2019). For these reasons we estimate that the current absolute accuracy of the iron scale is roughly ± 0.1 dex based on these three independent studies. Overall, we conclude that after the correction for different solar Fe abundances, our values are still 0.064 dex higher on average than the optical Carretta scale.

4.2 Intrinsic iron spread in clusters

We defined the RMS scatter (R_X, where X is the particular element) of each element or sum of elements as the standard deviation around the mean value in each cluster using the restrictions listed in Table 5. Detection of an intrinsic Fe abundance spread requires an accurate knowledge of the abundance measurement error within the sample. The rms and cluster average iron errors are listed in Table 3. The errors are underestimated when [Fe/H]<-1.6, and overestimated for most of the more metal-rich clusters, which is probably the result of over and underestimating the effect of some sources of error, like dependence on effective temperature, S/N etc. There are two obvious outliers when comparing errors to the internal spread: ω Cen and NGC 6229. ω Cen is well known to host multiple populations with an Fe spread (Johnson & Pilachowski 2010; Gratton et al. 2011). We believe that our errors on the metallicity for NGC 6229 are significantly underestimated because the spread of Fe is 0.128 dex, while the error is 0.038 dex, the lowest in our sample.

The RMS scatter in relation to the cluster age can be seen in the bottom left-hand panel of Fig. 5. We use a recent compilation of ages by Krause et al. (2016), which omits ω Cen from its sample. Alternatively one can use the ages from Marín-Franch et al. (2009), but results presented in this paper are not affected by the difference between these two ages. Table 6 contains the statistics of correlations

Table 6. Correlation of parameters with cluster properties.

Parameter Pair	N[a]	a	b	r	p-value	Comments
Fe average − Age	27	...	...	...	...	Non-linear correlation, Section 4.2.
Fe scatter − log(Mass)	30	− 0.002690	0.110497	− 0.0615	0.7468	No correlation, ω Cen not fitted.
Fe scatter − V_{Abs}	30	0.001578	0.108669	0.0915	0.6306	No correlation, ω Cen not fitted.
Fe scatter − Age	27	0.001722	0.074533	0.0884	0.6610	No correlation.
N_{SG}/N_{tot} − [Fe/H]	16	− 0.182509	0.249953	− 0.4899	0.0541	Weak/No correlation, Section 5.4.
N_{SG}/N_{tot} − log(Mass)	16	− 0.013256	0.613653	− 0.0348	0.8982	No correlation.
N_{SG}/N_{tot} − V_{Abs}	16	0.020454	0.710909	0.1328	0.6239	No correlation.
N_{SG}/N_{tot} − Age	15	0.105273	− 0.770896	0.6850	0.0048	Strong correlation, Section 5.4.
Al scatter − [Fe/H]	31	...	...	...	...	Non-linear correlation, Section 6.1.
Al scatter − log(Mass)	10	0.071677	0.054672	0.7426	0.0139	Moderate correlation, [Fe/H]<−1.5, Section 6.2.
Al corrected scatter − log(Mass)	9	0.099891	− 0.310714	0.8134	0.0077	Moderate correlation, [Fe/H]<−1.5, Section 6.2.
Al scatter − V_{Abs}	10	− 0.030952	0.190358	− 0.6809	0.0301	Moderate correlation, [Fe/H]<−1.5, Section 6.2.
Al corrected scatter − V_{Abs}	9	− 0.038668	− 0.082526	− 0.7091	0.0324	Moderate correlation, [Fe/H]<−1.5, Section 6.2.
Al scatter − Age	27	...	...	...	...	Non-linear correlation, Section 6.3.
Mg+Al+Si average − [Fe/H]	31	− 0.050382	0.640883	− 0.2851	0.1200	No correlation.
Mg+Al+Si average − log(Mass)	31	− 0.000689	0.713763	− 0.0041	0.9825	No correlation.
Mg+Al+Si average − V_{Abs}	31	0.002073	0.726658	0.0299	0.8731	No correlation.
Mg+Al+Si average − Age	27	0.053967	0.044826	0.6468	0.0003	Strong correlation, Section 6.4.
Mg+Al+Si scatter − [Fe/H]	31	− 0.016603	0.049214	− 0.3227	0.0767	Weak/No correlation, Section 6.4.
Mg+Al+Si scatter − log(Mass)	31	0.003140	0.055162	0.0641	0.7323	No correlation.
Mg+Al+Si scatter − V_{Abs}	31	− 0.001116	0.063077	− 0.0553	0.7689	No correlation.
Mg+Al+Si scatter − Age	27	0.006675	− 0.009527	0.2737	0.1671	No correlation.
N scatter − [Fe/H]	21	0.187394	0.52432	0.5341	0.0126	Moderate correlation, Section 7.2.
N scatter − log(Mass)	21	0.030739	0.144789	0.1367	0.5546	No correlation.
N scatter − V_{Abs}	21	− 0.012339	0.211891	− 0.1345	0.5611	No correlation.
N scatter − Age	17	− 0.024625	0.621128	− 0.2533	0.3266	No correlation.
C+N+O average − [Fe/H]	19	0.015709	1.88571	0.0431	0.8609	No correlation.
C+N+O average − log(Mass)	19	− 0.013718	1.94238	− 0.0650	0.7915	No correlation.
C+N+O average − V_{Abs}	19	0.015851	1.99543	0.1841	0.4506	No correlation.
C+N+O average − Age	16	0.060981	1.13055	0.6011	0.0138	Moderate correlation, Section 7.4.
C+N+O scatter − [Fe/H]	19	− 0.029856	0.085138	− 0.3024	0.2083	No correlation.
C+N+O scatter − log(Mass)	18	0.024809	− 0.017488	0.4207	0.0821	No correlation, ω Cen not fitted, Section 7.4.
C+N+O scatter − V_{Abs}	18	− 0.010535	0.031638	− 0.4656	0.0515	No correlation, ω Cen not fitted, Section 7.4.
C+N+O scatter − Age	16	− 0.006833	0.198537	− 0.24	0.3706	No correlation.

Notes. The correlation is determined by fitting the $f(x) = a \cdot x + b$equation. The *P*-value expresses the probability of getting a significant correlation if only numeric fluctuations were present and no signal.
[a]The number of clusters included in the statistics.

between metallicity and cluster parameters. The age–metallicity relationship shown in Fig. 5 is very similar to those of Marín-Franch et al. (2009) and Krause et al. (2016). We refer the reader to these papers to provide a detailed discussion on this topic.

The measured RMS as a function of the main cluster parameters, mass, absolute visual magnitude can be seen in Fig. 5. Carretta et al. (2009c) has reported that the iron spread is correlated with absolute visual magnitude and mass. From Fig. 5 we are not able to confirm this; we find that the spread of Fe does not depend on either the mass, absolute visual magnitude, or the age of the clusters (see Table 6 for statistical analysis). The lack of confirmation of the correlation may be due to our errors being slightly larger than that of Carretta et al. (2009c), although we believe our precision should be high enough to confirm such a correlation if it existed.

The iron spread in most clusters spans from 0.040 to 0.129 dex, with the exception of one cluster with 0.205 dex: ω Cen. Not counting ω Cen, the average spread of iron in 30 clusters is 0.096 dex. The true intrinsic iron spread can be computed by subtracting the effect of random error of the average value in quadrature from the measured cluster Fe RMS. As mentioned before, our estimated errors can technically be somewhat smaller or larger than the measured scatter, here, the average level of the error is assumed to be equal to the scatter for simplicity. With this simplification the true real iron spread is around 0.068 dex on average across 30 clusters. Carretta et al. (2009c) reported an average iron spread value of 0.048 dex based on 19 GCs, and our value is 0.065 dex for the 17 clusters in common with that sample. Our study is lower resolution than Carretta et al. (2009c), which is the most likely source of our slightly higher internal errors.

While it is widely known that ω Cen has a significant spread in iron that is of astrophysical origin (e.g. Johnson & Pilachowski 2010), other clusters have been reported to have a significant spread, but this does not appear in our measurements. From the overview of Da Costa (2016) these clusters are: NGC 1851, ω Cen, NGC 362, NGC 5286, NGC 5824, M19, M22, M54, M75, and M2. Our data set includes five of those clusters. The iron spread in M22, M2, NGC 362, and NGC 1851 has been debated later, in particular because they can be introduced artificially by how

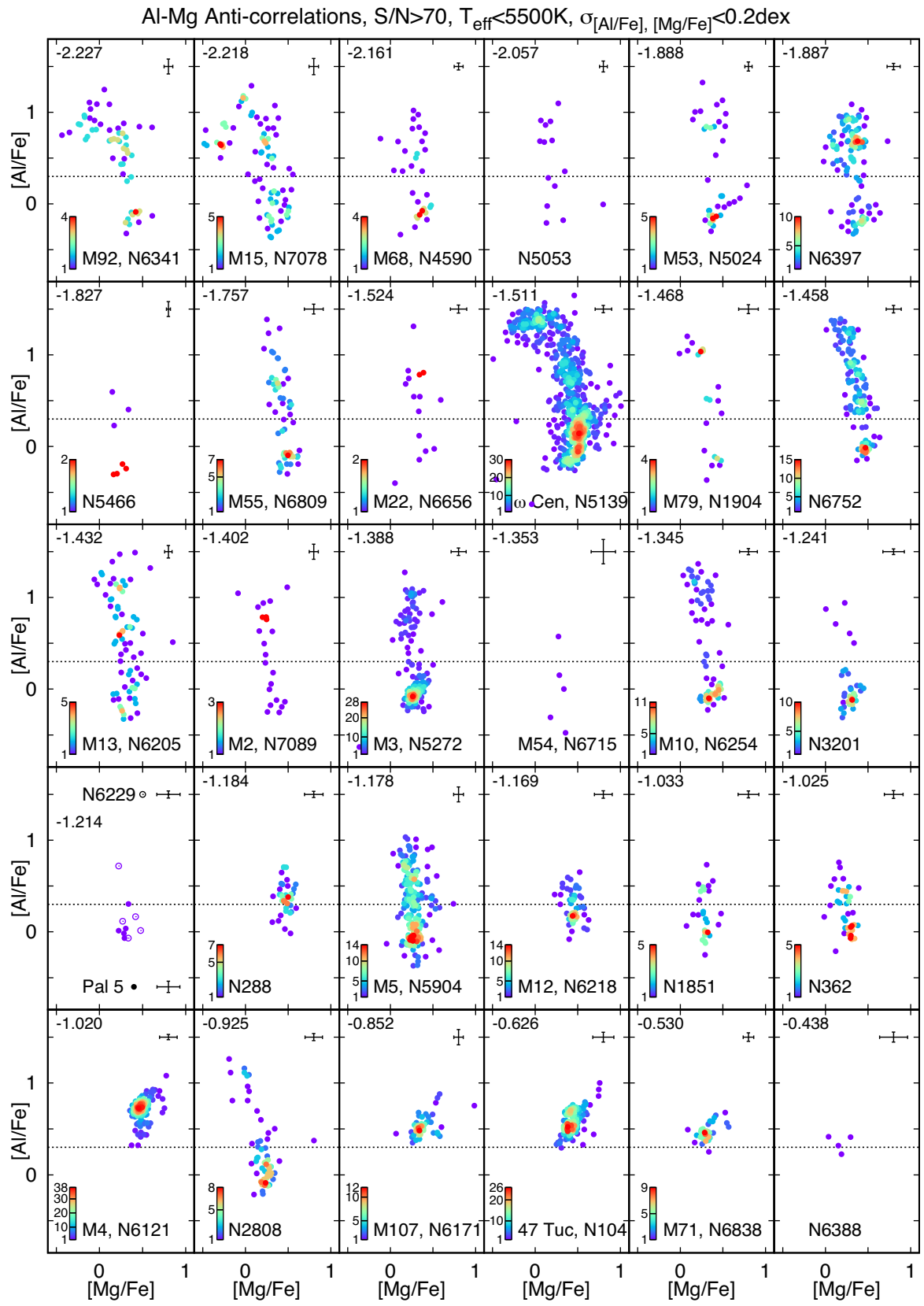

Figure 6. Al-Mg anticorrelations in 31 clusters, NGC 6229 and Pal 5 are plotted in the same panel for simplicity. Each panel is colour-coded linearly by the density of points calculated in a ±0.05 dex range around each point. The colour legend shows the density range for each cluster. The dotted line drawn at [Al/Fe] = 0.3 dex denotes a generalized separation of classic first- and second-generation stars. Clusters are ordered by decreasing average metallicity, which is indicated in the top left-hand corner in each panel.

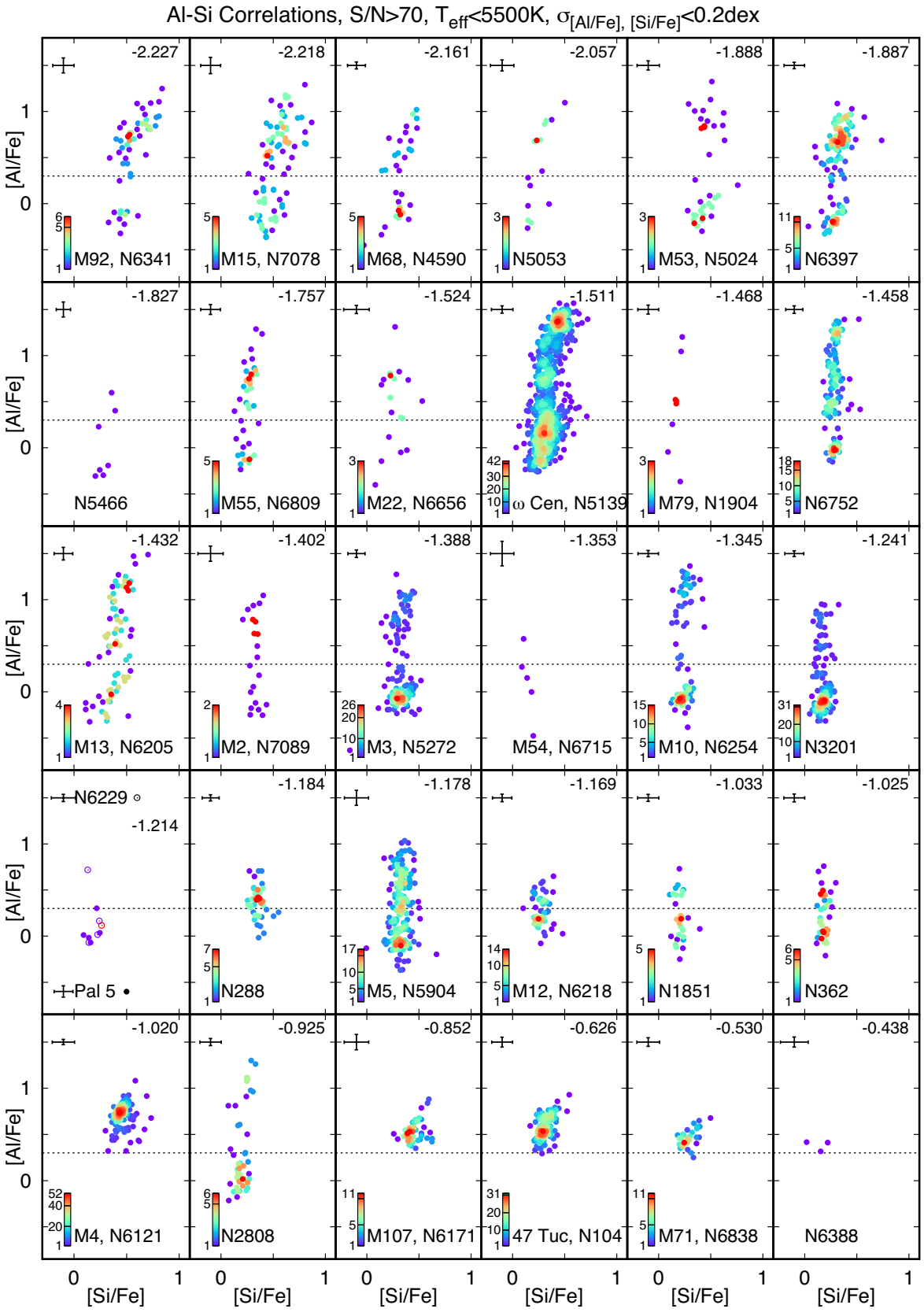

Figure 7. Al-Si correlations in 31 clusters. The meaning of colour legends and the line drawn at [Al/Fe] = 0.3 dex are the same as in Fig. 6. Clusters are ordered by decreasing average metallicity, which is indicated in the top right corner in each panel.

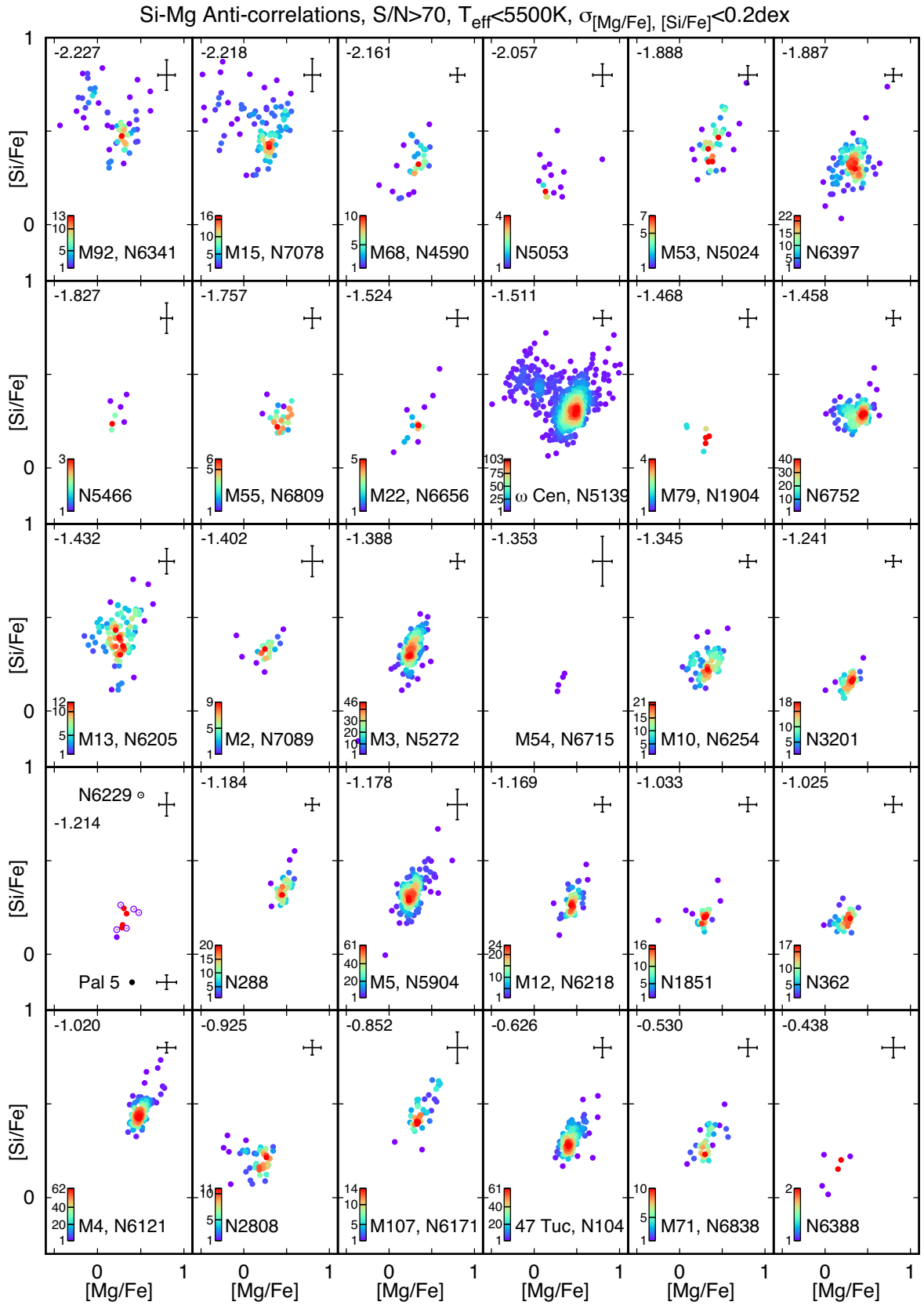

Figure 8. Mg-Si anticorrelations in 31 clusters. Clear anticorrelation can be seen in only three clusters: M92, M15, and ω Cen. Clusters are ordered by decreasing average metallicity, which is indicated in the top left-hand corner in each panel.

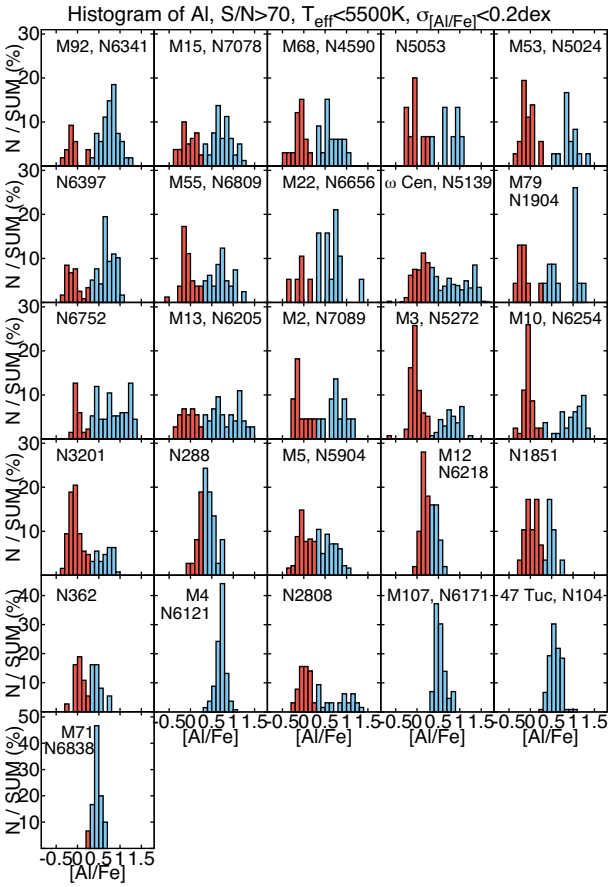

Figure 9. The histogram of Al distribution in 0.1 dex bins. Stars with [Al/Fe]<0.3 dex are denoted by red, stars with [Al/Fe]>0.3 dex with blue to indicate classic FG/SG separation.

atmospheric parameters were derived for those studies (Mucciarelli et al. 2015b; Lardo, Mucciarelli & Bastian 2016). In ω Cen, which has a wide metallicity distribution, we find an Fe scatter of 0.2 dex, clearly above our errors. M2 has a range in metallicity (Yong et al. 2014; Lardo et al. 2016), with a high-metallicity population at [Fe/H]~-1.0 that comprises only 1 per cent of the cluster. Our measured Fe scatter in M2 is 0.06 dex, which is consistent with having observed entirely stars from the dominant population. All four of these clusters (M22, M2, NGC 362, NGC 1851) show Fe spreads expected from our internal errors (see Table 3 for individual values), and while our measurements do not disagree with the literature, we cannot make strong statements about the intrinsic Fe scatter in these four clusters. APOGEE observed only seven stars with S/N > 70 in M54, a sample not large enough to confirm or deny the broad metallicity distribution reported by Carretta et al. (2010a). Terzan 5 was also reported to have a multimodal metallicity distribution (Massari et al. 2014), but this cluster was excluded from our analysis due to large uncertainties in $T_{\rm eff}$ coming from its very high reddening.

5 MULTIPLE POPULATIONS BASED ON AL AND MG

5.1 The Al-Mg anticorrelation

It has been shown by several groups (e.g. Carretta et al. 2009a,b; Gratton, Carretta & Bragaglia 2012) that variations in C, N, O, and Na can be seen in all observed GCs, but this is not the case for Al and Mg. The Mg-Al cycle needs large temperatures (>70 million Kelvin) to operate, temperatures that only the core of low metallicity polluters are capable of reaching. This is reinforced by the observation that some metal-rich clusters can be described by one single [Al/Fe] value, while in others the variation in the Al content spans a large range, as first reported by Shetrone (1996). We are able to discuss the dependence of the shape of Al-Mg on cluster parameters in more detail than it was possible before due to the increased number of observed clusters with a sufficient number of stars.

In this paper we discuss the largest sample of the Al-Mg anticorrelation and Al-Si correlation to date in 31 clusters, plotted in Figs 6, 7, and 8, in which the clusters are ordered by decreasing metallicity. An anticorrelation between Al and Mg is weakly present in most clusters, with a typical Mg range is $0.2 < [\rm Mg/Fe] < 0.6$ dex, much smaller than that of Al. RGB and AGB stars do not appear to follow different paths, or group separately in any of the abundance–abundance figures presented in the paper. There are two clusters shown here that have had no Al-Mg anticorrelation investigated before: NGC 6229 and Pal 5. While we have only five members in each of the three clusters that make our parameter cuts, it is enough to observe elevated Al abundances showing the signs of the Mg-Al cycle. It is clear that the extended distribution of Al, which is much

Table 7. The description of MPs based on the Al distribution.

ID	Name	N_P	Description
NGC 104	47 Tuc	1	no Al spread
NGC 288		2?	small Al spread
NGC 362		2	small Al spread
NGC 1851		2	small Al spread
NGC 1904	M79	3	trimodal, but need more data
NGC 2808		2	continuous
NGC 3201		2	bimodal/continuous?
NGC 4590	M68	2	bimodal
NGC 5024	M53	2	bimodal
NGC 5053		2?	bimodal, but need more data
NGC 5139	ω Cen	3	continuous with density peaks
NGC 5272	M3	2	bimodal
NGC 5466		···	not enough data
NGC 5904	M5	2	continuous
NGC 6121	M4	1	no Al spread
NGC 6171	M107	1	no Al spread
NGC 6205	M13	2	continuous with density peaks
NGC 6218	M12	2?	small Al spread
NGC 6229		···	not enough data
NGC 6254	M10	2	bimodal
NGC 6341	M92	2	continuous with gap and Al turnover
NGC 6388		1	no Al spread, but need more data
NGC 6397		2	bimodal
NGC 6656	M22	···	not enough data
NGC 6715	M54	···	not enough data
NGC 6752		4	continuous with gap and density peaks
NGC 6809	M55	2	continuous with gap
NGC 6838	M71	1	no Al spread
NGC 7078	M15	2	continuous with Al turnover
NGC 7089	M2	2	continuous, but need more data
Pal 5		···	not enough data

Notes. The number of populations was determined using the distribution of Al abundances only. The most metal-rich clusters have no Al spread, but still have large *N* variations proving the existence of MPs. See Sections 5.1 and 6.2 for more discussion.

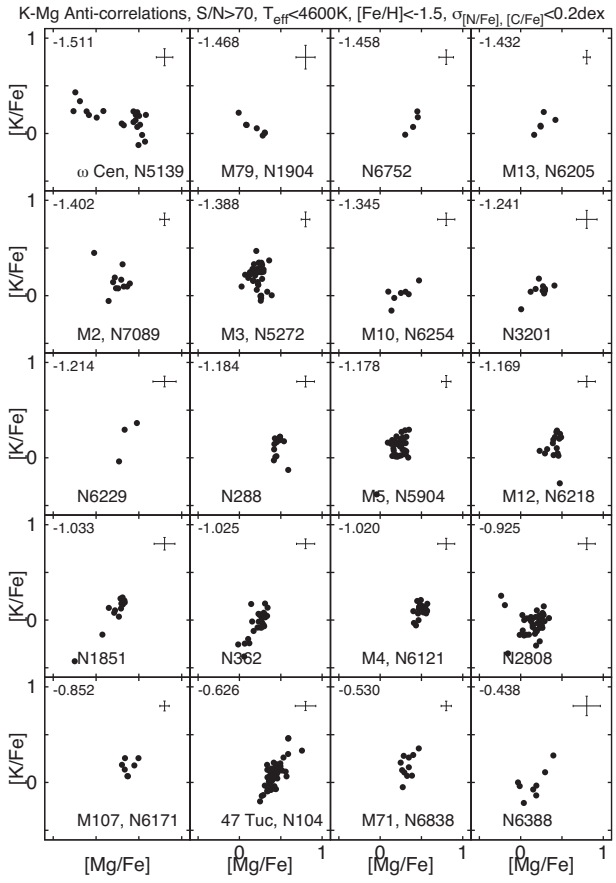

Figure 10. Mg-K anticorrelations in 20 clusters. An anticorrelation might be observed in three clusters only: M79, NGC 2808, and ω Cen. Clusters are ordered by decreasing average metallicity, which is indicated in the top left-hand corner in each panel.

larger than the typical errors of [Al/Fe] and [Mg/Fe], is present in most metal-poor clusters, and clearly shows the past presence of the Mg-Al cycle. Mészáros et al. (2015) used an extreme-deconvolution method to identify population groups based on Mg, Al, Ca, and Si abundances. They found that it was Al abundances that drive the separation between stars, and northern clusters (except M107 and M71) presented in that paper could be divided into only two populations corresponding to first- and second-generation stars. Because an initial separation of FG and SG stars can be simply done by setting the [Al/Fe] limit at around 0.3 dex, we opted against doing a detailed population analysis again based on the same method, and instead use density maps and histograms of Al to explore MPs in all clusters. This is further motivated by the fact that most of the clusters show bimodal or continuous distributions in Al, in the latter selecting groups will always be difficult. While it is certainly possible that more than two populations are present in all of these clusters, their effect in the distribution of Al can be blurred out by any bias in target selection, and/or any measurement error we have, even if those are smaller than 0.1 dex in most cases. We set a limit of [Al/Fe] = 0.3 dex to act as a guide to quickly and easily separate FG and SG stars. This limit is drawn in both Figs 6 and 7.

Instead of colouring the Al-Mg and Al-Si plane according to population, we colour them by their respective density calculated in a $\pm$0.05 dex range around each star. While this colouring method does not provide significant information if the number of stars in a cluster is small (NGC 5466, M54, Pal 5, NGC 6229, NGC 6388), our sample is large enough in most clusters to use this as a tool of analysing multiple populations in GCs instead of the previously mentioned extreme-deconvolution method. This is further motivated by the findings of Carretta et al. (2012) in NGC 6752 for which multiple populations manifested themselves in the enhancement and depletion around discrete abundance values in an otherwise rather continuous distribution. In clusters that are considered to have one population with enriched [Al/Fe] values, or where the scatter of Al is smaller than 0.2 dex, the density profile also shows that most stars are concentrated around a single value of [Al/Fe]. These are the metal-rich clusters M4, M107, 47 Tuc, and M71.

On the other hand, clusters with scatter of Al larger than 0.4 dex have vastly different density profiles even compared to each other. In some GCs the FG stars are concentrated around one single value of Al, like in ω Cen, NGC 6752, M3, M10, M5, NGC 3201, NGC 2808, and perhaps M68. Other GCs with extended Al distribution do not show this behaviour so clearly: M15, M92, M79, M2, M13, M55, and M53. The reason behind this varies from cluster to cluster. In M15 and M92, the [Mg/Fe] distribution of the FG stars is more sparse than in the more metal-rich clusters smoothing out any obvious density peaks. M79 and M2 may have too few stars observed in them to make a definite conclusion. M13 has a clear continuous distribution of Al abundances with no density peak in its FG stars, while M55 and M53 show only a small density peak below [Al/Fe]<0.3 dex. It appears that there is no clear correlation between the cluster metallicity, or the shape of the Al distribution and the existence of a density peak inside the FG stars.

The histogram of Al can corroborate the findings from the density maps by integrating any spreads coming from Mg and Si together. This histogram is plotted in Fig. 9 using δ[Al/Fe] = 0.1 dex bins for clusters with significant number of stars observed. The histogram is normalized in each panel to the total number of stars in each cluster. While the density plots give more detail, the advantage of the histogram is that it can give a more complete picture if we have reliable [Al/Fe] abundances, but Mg or Si measurements are missing, like in NGC 3201 in which several Al rich stars do not have measurements of [Mg/Fe] or [Si/Fe]. When analysing the number of populations in each cluster we use the density maps in Figs 6 and 7 and the histogram in Fig. 9 in a complementary fashion. Table 7 summarizes how many populations were identified in each cluster based on these methods and provides a short description of the Al distribution.

Both Carretta et al. (2009a) and Mészáros et al. (2015) have reported observing bimodal and continuous distributions of Al. Our extended sample of stars and clusters paint a more complex picture on the distribution of Al by smoothing out the differences between bimodality and continuousness. For example, Mészáros et al. (2015) observed a clear bimodality in M3 and M53, but the distribution in the current (larger) sample is more continuous. On the other hand, M53 is still clearly bimodal. The classical bimodality/continuous distinction is further complicated by the fact that there are several clusters with continuous distribution of Al, but with well-defined Al-Mg density peaks: ω Cen, NGC 6752, and perhaps M13. Another interesting observation in both bimodal and continuous clusters is the existence of a gap with no or very few stars between [Al/Fe] = 0.1 and 0.3 dex. The following clusters meet this criterion: M10, M3, NGC 6752, M55, NGC 6397, M53, M68, M92. NGC 6752 is particularly interesting, because it exhibits multiple of these properties, it has an extended and continuous SG distribution with four density peaks that is separated from the FG stars by an 0.2 dex wide almost empty gap. This also confirms and adds one

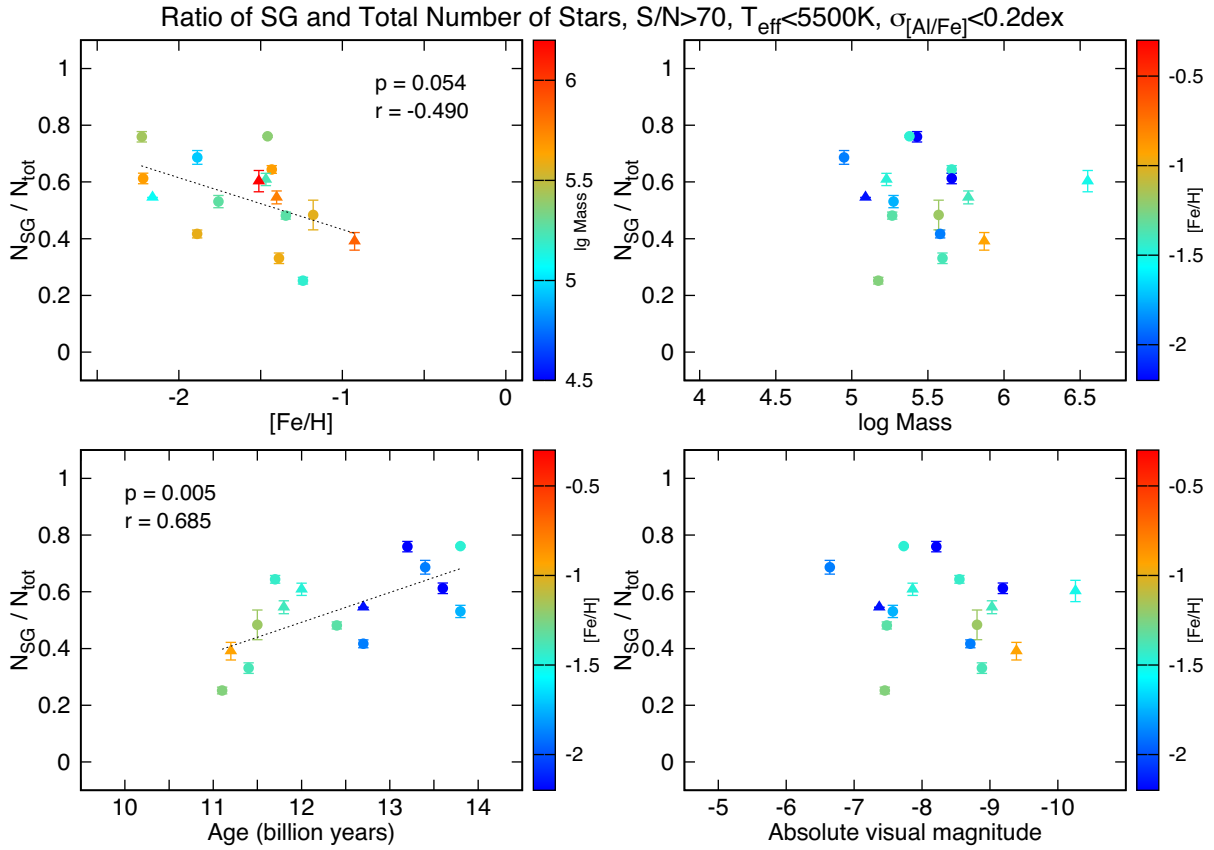

Figure 11. The ratio of the number of FG and SG stars as a function of cluster parameters. Accreted clusters are denoted by triangles, *in situ* clusters by solid circles. The most metal-rich GCs are not included because those exhibit one single population based on Al alone.

more population to the results by Carretta et al. (2012), who has found three populations using [Al/Fe] in an otherwise continuous Al distribution. Based on these observations it is clear that it is hard to generalize MPs from the properties of Al-Mg, and in reality every cluster has its own specific pattern of MPs showing a high degree of variety.

5.2 The presence of Si-Mg anticorrelation

Weak Si-Mg anticorrelations were observed in a small number of massive and metal-poor GCs before: NGC 6752 (Yong et al. 2005), NGC 2808, and M15 (Carretta et al. 2009a). This implies leakage from the MgAl chain into Si production through the ^{26}Al(p,γ)^{27}Si(e-,ν)^{27}Al(p,γ)^{28}Si reactions at high temperature. Without this leakage, we would expect a simple correlation between Mg and Si since they are both alpha elements.

From Fig. 8 we are able to confirm the Si-Mg anticorrelation observed in NGC 2808 by Carretta et al. (2009a), but the case of NGC 6752 (as observed by Yong et al. 2005) is less convincing. Although some stars seem to have lower Mg abundances, [Mg/Fe]<0.2, than where the most part of the cluster lies at [Mg/Fe]>0.3, these stars do not show larger Si abundances than their Mg-rich counterparts. Thus, our data do not confirm the occurrence of hot proton burning in the early populations of NGC 6752.

An Al-Si correlation in M15 and M92 was also observed by Mészáros et al. (2015), but it was Masseron et al. (2019) who has discovered more stars in M15 and M92 that show an extreme Mg depletion with some Si enhancement while at the same time Al depleted relative to the most Al-rich stars in these clusters, displaying an unexpected turnover in the Mg-Al diagram.

In this paper we present the same type of behaviour of the Al-Mg anticorrelation in ω Cen shown in comparison with M15 and M92 in Fig. 6. It can be clearly seen that the most extreme Mg-poor stars in ω Cen have lower Al content than what is expected from the traditional shape of the Al-Mg anticorrelation, while they are also the most Si-rich stars in the cluster. The Si-Mg anticorrelation is clear in all of these three clusters (Fig. 8). Masseron et al. (2019) explained the shape of Al-Mg by suggesting that Al has been partially depleted in their progenitors by very hot proton-capture nucleosynthetic processes occurring above 80 MK temperatures. While M15 and M92 are two of the most metal-poor clusters, ω Cen is significantly more metal-rich, showing that the observation of the turnover of the Al-Mg diagram at different metallicities may be the result of multiple mechanisms. Because this paper focuses on the overall characteristics of globular clusters, the detailed discussion of ω Cen is out of the scope of this study. We will present the detailed analysis of ω Cen in the third part of our series.

5.3 The presence of K-Mg anticorrelations?

Stars showing a large range of K abundances were first discovered by Mucciarelli et al. (2012) in NGC 2419. Later, Mucciarelli et al. (2015a) observed a large K enhancements in four stars with very low Mg abundances in NGC 2808. The enhancement of K is currently not understood. Ventura et al. (2012) attempted to explain the origin of a Mg-K anticorrelation by suggesting that this population might

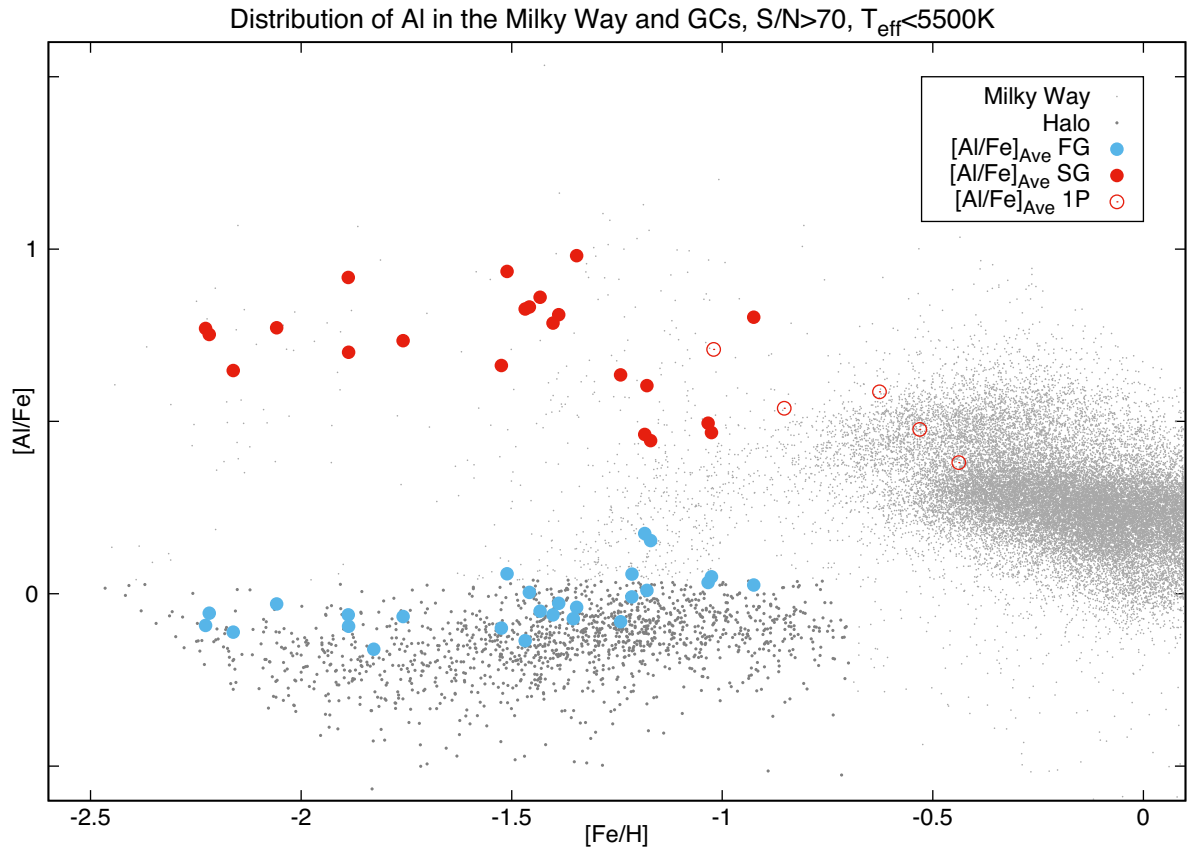

Figure 12. Chemical evolution of Al in the Milky Way. The small grey dots are standard Milky Way stars, dark grey dots are stars mostly from the Galactic Halo. The blue dots denote the average [Al/Fe] of the FG stars with [Al/Fe]<0.3 dex, red dots denote the average [Al/Fe] of the SG stars with [Al/Fe]>0.3 dex. The open red dots show the clusters that do not show signs of Al enrichment due to pollution.

have directly formed from super-AGB ejecta. NGC 2419 is not in our sample so we can only examine the existence of K-rich stars in NGC 2808, as shown in Fig. 10. Our confirmation is based on two stars with very low, [Mg/Fe]<0.0 dex, Mg abundances that are slightly enhanced in K compared to the more Mg rich, mostly FG stars.

Interestingly, ω Cen contains seven stars with [Mg/Fe]<0.0 dex, previously discussed in Section 5.2, that are also slightly enriched in K compared to the classical FG stars, drawing a weak anticorrelation between K and Mg in Fig. 10. However, the two K lines found in the *H*-band are fairly weak at low metallicities and high temperatures (they are also often blended), thus it is necessary to implement a strict cut on these two parameters (Table 5) to cut out upper limits, even when BACCHUS reports real detection. Considering these issues, our conclusion is that the discovery of K enhancement of the Mg-poor stars in ω Cen cannot be convincingly claimed from our spectra, the anticorrelation is weak and we need independent confirmation from optical spectra before the extent of the enhancement can be reliably discussed.

There is another cluster in our sample, M79, which shows a weak K-Mg anticorrelation shown in Fig. 10, although the extent of the Mg abundances in the M79 are on the level of the reported uncertainties. In such a case the observed anticorrelation is more likely the result of correlated errors, and not of an astrophysical origin.

The weak correlation between Mg and K observed in NGC 1851, NGC 362, and 47 Tuc exists because there are 2–3 outlier stars with very high or very low [K/Fe] abundances in each of these clusters, which are most likely bad abundance determinations.

5.4 The ratio of FG and SG

The discussion of the ratio of SG versus FG stars is generally difficult because there needs to be a significant number of stars observed in each cluster. For this reason we limit our discussion to clusters that have at least 20 stars observed. As in photometric studies such as Milone et al. (2017), we use the definition $f_{enriched} = N_{SG}/N_{tot}$ to examine the extent of enrichment. The computed $f_{enriched}$ ratios can be found in Table 3. When calculating the number of FG and SG stars we used the limit of [Al/Fe] = 0.3 to separate FG and SG stars. However, error bars were computed by varying the limit from 0.25 to 0.35 dex and the ratio recalculated. The $f_{enriched}$ ratio is plotted against the cluster properties in Fig. 11. The resulting error bars are generally small and do not affect any conclusion on how the ratio depends on cluster parameters.

We listed the statistics of the $f_{enriched}$ correlation with cluster properties in Table 6. A very weak, statistically barely significant with p = 0.0541, linear correlation was found against metallicity, in which more metal-poor clusters exhibit more SG stars than FG stars. Considering that the ratio can be improved by observing more stars, this correlation may move closer to or farther from statistically significant, but in this paper we do not explicitly conclude that this correlation exists. The correlation is similar to what Bastian &

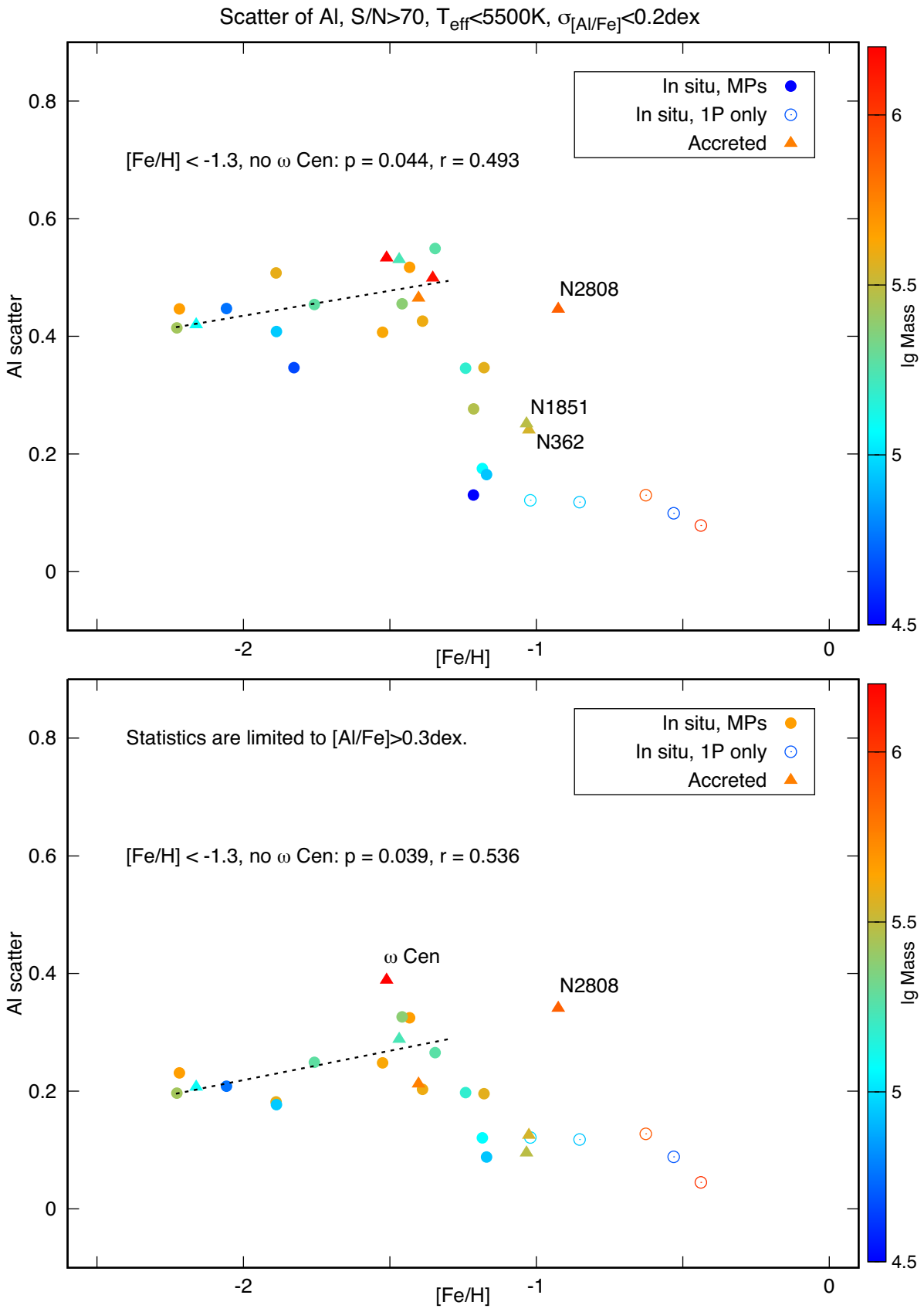

Figure 13. Scatter of Al as a function of average cluster [Fe/H] colour coded by mass for clusters with at least three members. Accreted clusters are denoted by triangles, *in situ* clusters by solid circles. Top panel shows R_{Al} as directly observed, the bottom panel shows the scatter of Al after excluding the FG stars with [Al/Fe]<0.3 dex from the sample. See Section 5.1 for discussion.

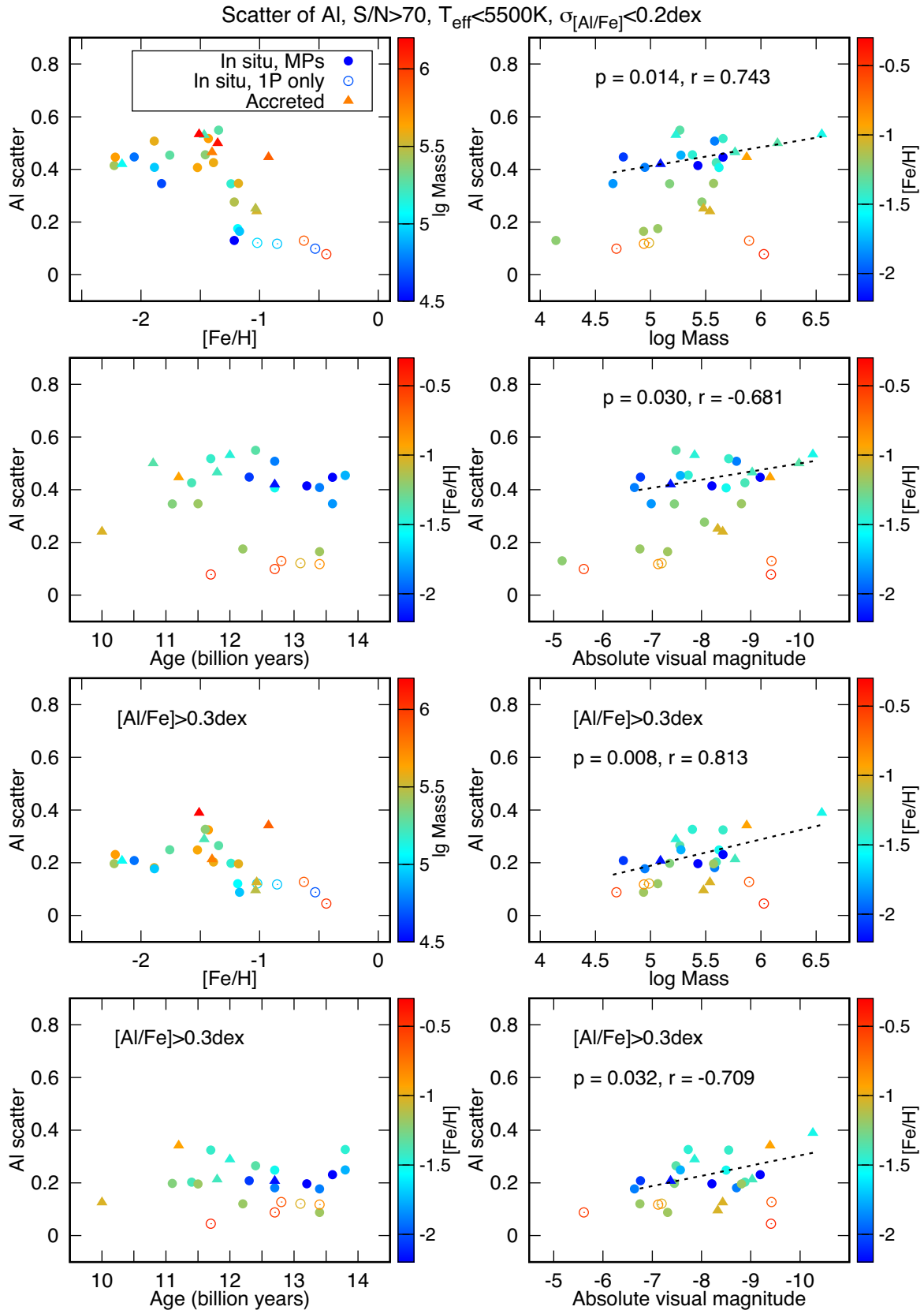

Figure 14. Scatter of Al as a function of cluster parameters for clusters with at least three members. Accreted clusters are denoted by triangles, *in situ* clusters by solid circles. The top four panels show R_{Al} as directly observed, the bottom four panels show the scatter of Al after excluding the FG stars with [Al/Fe]<0.3 dex from the sample. See Section 5.1 for discussion.

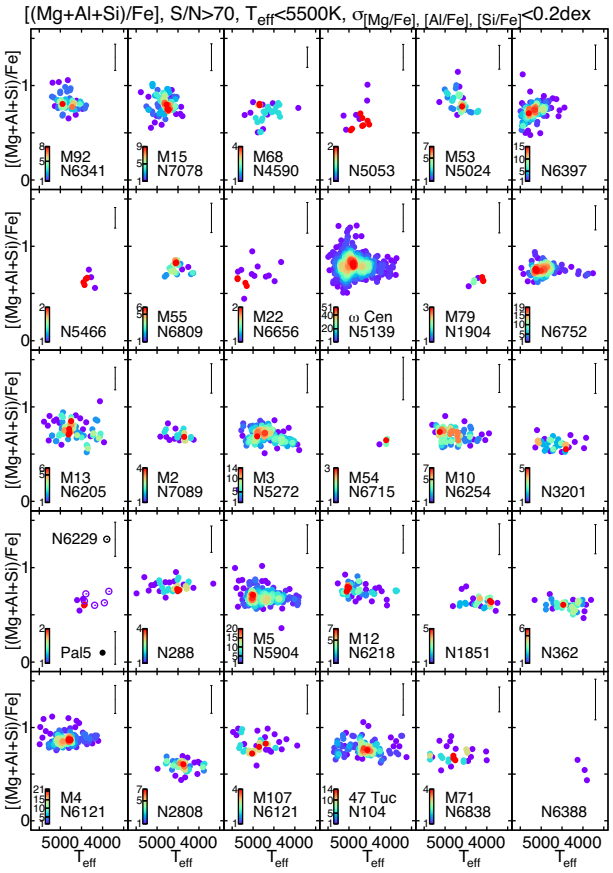

Figure 15. Mg+Al+Si as a function of effective temperature. Each cluster exhibits the same [(Mg+Al+Si)/Fe] value across MPs.

Lardo (2015) have found using spectroscopic results collected from the literature, which has been confirmed by Milone et al. (2017) with the *HST* Legacy Survey (Piotto et al. 2015; Soto et al. 2017). The only clear and statistically significant correlation ($p = 0.0048$) is with cluster age, with the younger clusters exhibiting lower $f_{enriched}$ than the older ones.

In terms of absolute values of $f_{enriched}$ we have a good agreement with Milone et al. (2017) as both studies measured $f_{enriched}$ between 0.4 and 0.8 for most clusters. However, a correlation with mass and absolute visual magnitude is non-existent in our data, which is in sharp contrast with what Milone et al. (2017) observed. They observed that more massive clusters have more SG stars than less massive ones. Our study is biased towards the outer cluster regions, because the fibre-collision radius does not allow the APOGEE instrument to properly sample the inner regions. The *HST* data samples the inner 2 arcmin of the clusters, thus there are very few stars which overlap between APOGEE and *HST* observations (Mészáros et al. 2018). The significant difference between our correlations with $f_{enriched}$ and that of Milone et al. (2017) may arise from cluster properties which depend on distance from the cluster core.

6 THE SPREAD OF AL ABUNDANCES

In order to properly discuss the Al scatter as a function of cluster parameters, we need to distinguish between clusters that form *in situ* with the Milky Way and those that were accreted by the Milky Way. In the most recent models, the haloes of galaxies similar to the Milky Way are believed to be formed from the accretion of smaller galaxies (Bullock & Johnston 2005; Abadi, Navarro & Steinmetz 2006; Font et al. 2006). These small dwarf galaxies are disrupted and incorporated into the larger galaxy, only very dense components like globular clusters will survive intact (Peñarrubia, Walker & Gilmore 2009). The GCs that are formed from this accretion process are then added to the rest of the clusters formed *in situ* within the Milky Way. There have been several efforts made to identify these accreted clusters (*Gaia* sausage clusters, CMa and Sag clusters, Sequoia clusters), but the following are in common with our sample: NGC 1851, NGC 1904, NGC 2808, NGC 362, NGC 7089 (Forbes & Bridges 2010; Myeong et al. 2018), NGC 4590 (Forbes & Bridges 2010), and ω Cen (Bekki & Freeman 2003).

It is also important to take the standard chemical evolution of the Milky Way into account, which was explored by Hayes et al. (2018) using APOGEE DR13 data. This is illustrated in Fig. 12, in which we plotted the average [Al/Fe] of FG and SG stars as defined in Sections 5.1 for all clusters with at least three members in each population on top of stars observed in the Galaxy. Stars from the Milky Way were selected by applying the criteria defined by Hayes et al. (2018) to the DR14 data. The average [Al/Fe] of FG stars (blue dots) agree well with the Al abundances observed in the Galactic halo, denoted by dark grey points, while the average [Al/Fe] of SG stars is elevated (red dots). The slight, roughly 0.1 dex systematic offset between the average [Al/Fe] of FG stars and the [Al/Fe] of Galactic halo stars is most likely due to systematics between BACCHUS and ASPCAP, the latter used by Hayes et al. (2018). As metallicity increases, the two averages get closer to each other. The metal-rich clusters (red open dots) that only show a single Al population with an average [Al/Fe] close to what is observed in the Galactic thick and thin disc. The fact that the average [Al/Fe] of the FG is lower at low metallicities may introduce a bias to how the scatter of Al depends on cluster parameters. This is because metal-rich clusters formed in parts of the Galaxy where more Al was present to begin with.

We defined the RMS scatter of Al (R_{Al}) as the standard deviation around the mean value of [Al/Fe] in each cluster. Another measure that can be introduced is the difference between the maximum and minimum value of an abundance inside a cluster. This measure is less robust as it is more sensitive to any biases in target selection and less accurate when only a small number of stars are observed. As a test, we carried out the same statistical analysis of correlations by using both the scatter and the max−min of [Al/Fe] and found that the main conclusions are the same in both cases, but the relationships when using the max−min of [Al/Fe] are less defined and more noisy. For this reason we limit our discussion in Section 6 to that of R_X only.

6.1 Metallicity

As of now only a handful of studies have examined the behaviour of Al spread as a function of cluster parameters. As previously mentioned in Section 5.1, Carretta et al. (2009a), Mészáros et al. (2015), Pancino et al. (2017), Masseron et al. (2019), and Nataf et al. (2019) have reported that the extent of the Al distribution linearly depends on cluster metallicity, but all of those studies were carried out using only a handful of clusters or spanned a relatively small metallicity range, and did not take the evolution of Al in the Milky Way (Hayes et al. 2018) into account. Here, we are able to significantly increase the sample size to 31 clusters, and also cover a large metallicity range between [Fe/H] = −2.23 and −0.44 dex. Fig. 13 shows the measure RMS scatter of Al (R_{Al}) as a function of cluster average metallicity. The observed distribution of Al scatter is more complex than previously found, but it is also biased because

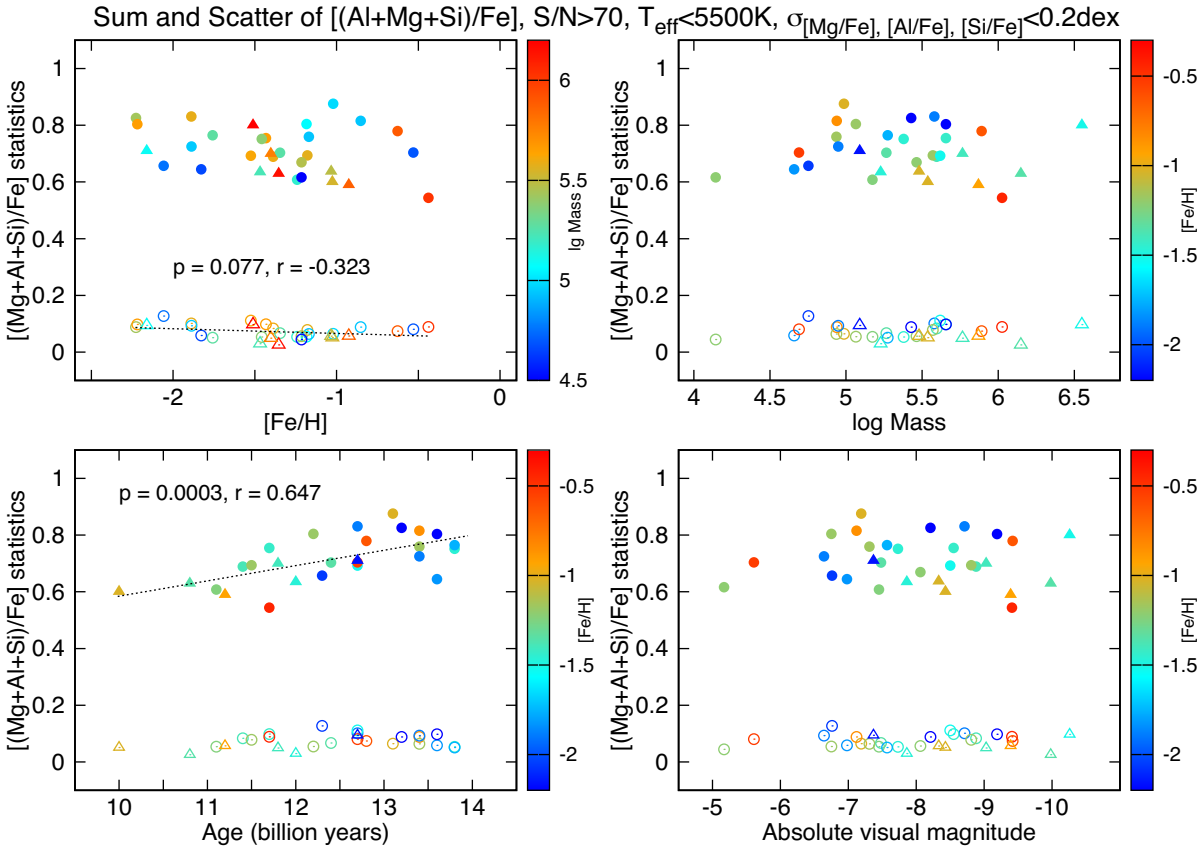

Figure 16. Statistics of Mg+Al+Si as a function of cluster [Fe/H] and mass. The filled symbols represent the average of Mg+Al+Si, the open symbols represent the scatter of Mg+Al+Si. The triangles are accreted clusters.

low metallicity halo stars have lower [Al/Fe] content than high metallicity disc stars (Hayes et al. 2018).

Based on the top panel of Fig. 13 there are three main groups that can be identified:

(i) [Fe/H] < -1.3: The scatter of Al in all clusters is larger than 0.35 dex. These clusters show clear Al-O, Al-N (anti)correlations (see Section 7.2). In this metal-poor region the correlation between [Fe/H] and R_{Al} is statistically significant but weak. Accreted clusters have very similar R_{Al} to that of those formed *in situ*.

(ii) $-1.3 >$[Fe/H] < -1.0: In this transition region there is a sharp drop of R_{Al} from about 0.5 to 0.18 dex. Here, accreted clusters are not present in our selection. These clusters also show clear Al-O, Al-N (anti)correlations.

(iii) [Fe/H] > -1.0: The R_{Al} is constant as a function of [Fe/H], and remains lower than 0.18 dex. However, there is a significant difference between the accreted GC NCG 2808 and other clusters. NCG 2808 has significantly higher R_{Al} than its *in situ* and other accreted counterparts with similar metallicity. Other than NGC 2808, none of these clusters have any Al-O, Al-N (anti)correlations.

The average error of [Al/Fe] spans a range from 0.03 to 0.09 dex, except for M54 for which $\sigma_{[Al/Fe]} = 0.13$, which is roughly half of the R_{Al} measured when [Fe/H]>-1.0. Considering that the calculated R_{Al} is the quadratic sum of the intrinsic Al spread and the error, the logical conclusion would be that these clusters do not bear the signs of past Al-Mg cycles in the progenitors. We believe this is not the case, because abundance is measured on a logarithmic scale, a larger absolute enrichment is required to see the same change in [Al/Fe] in metal-rich clusters than in metal-poor clusters. We provide more discussion on this topic in Section 7.3. It is important to note that the three accreted clusters (NGC 362, NGC 1851, NGC 2808) are among the most metal-poor ones in this third group of otherwise metal-rich GCs, meaning they may more naturally belong to the transition metallicity zone where R_{Al} drops suddenly. Nevertheless, accreted clusters with Al spreads close to the estimated errors are not observed.

As mentioned before, this picture may be biased because metal-rich clusters have an initial composition more Al-rich than metal-poor clusters due to chemical evolution in the Galaxy seen in Fig. 12. What we want to know is how the extent of the enrichment of GC stars depends on cluster parameters if we remove the effect of Galactic chemical evolution on the FG Al abundance.

In order to compensate for the chemical enrichment and to compute the scatter of Al more objectively, we exclude all stars from the sample that have [Al/Fe]<0.3, this is shown in the bottom panel of Fig. 13. This is possible taking into account that the Al production is more sensitive to the abundance of Mg available for the proton capture channel $^{25}Mg(p,\gamma)^{26}Al$ than to the initial Al abundance. After removing the bias introduced by the standard chemical evolution, the correlation of the [Fe/H]<-1.3 region remains the same and barely statistically significant, but the difference in R_{Al} between metal-rich and metal-poor clusters decreases significantly. The overall trend over the full metallicity range still shows that low metallicity clusters have higher Al scatter than the metal-rich ones.

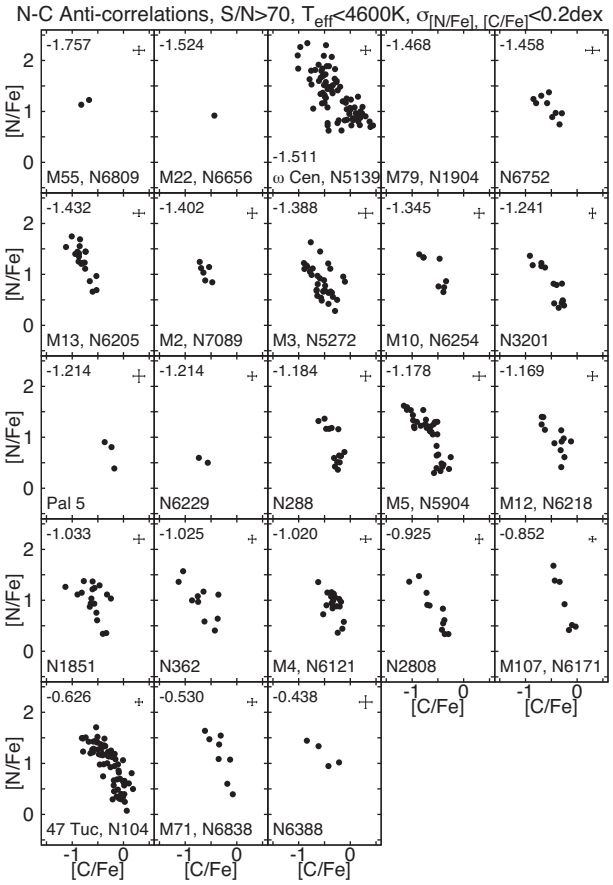

Figure 17. N-C anticorrelations. Most clusters show continuous distributions, only M10 and NGC 288 exhibit clear bimodality. Clusters are ordered by decreasing average metallicity, which is indicated in the top left-hand corner in each panel.

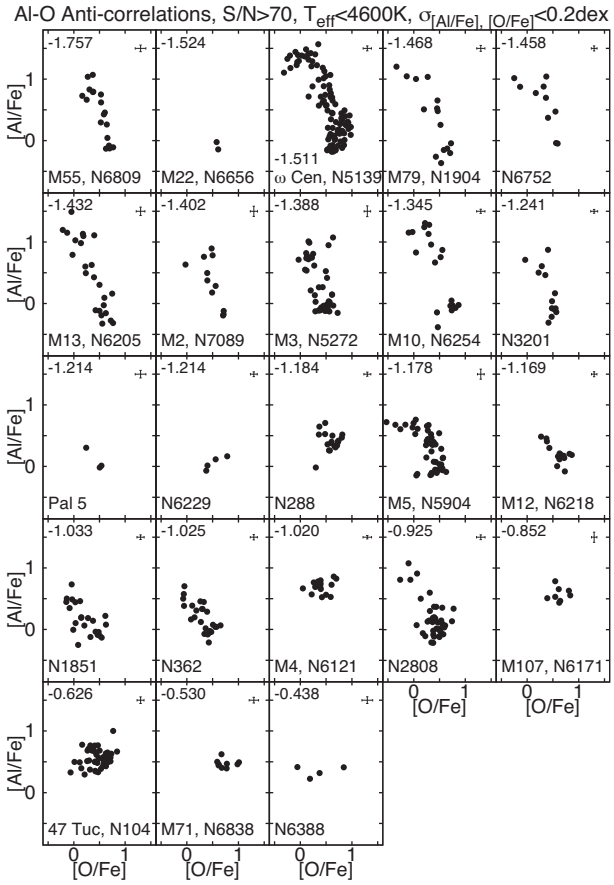

Figure 18. Al-O anticorrelations. All cluster show clear Al-O anticorrelations, except 47 Tuc, M4, M107, NGC 6388, and M71, cluster with no significant Al spread. Clusters are ordered by decreasing average metallicity, which is indicated in the top left-hand corner in each panel.

However, there are two outliers after the correction, ω Cen and NGC 2808, that lie above other GCs at similar metallicities, showing larger Al enrichment than expected. We know that NGC 2808 and ω Cen are among the most massive clusters and to properly discuss their behaviour one has to look at the mass dependence first.

6.2 Mass and V_{ABS}

Carretta et al. (2010b) used 19 GCs to look for correlations between the extent of the Na-O anticorrelation and cluster properties. The strongest relation found was with cluster mass, with higher mass clusters showing larger Na-O abundance spreads. A similar positive correlation between He spread and mass was found by Milone (2015) in which higher mass cluster exhibit larger He spreads. Looking at Al-Mg, both Carretta et al. (2009a,b) and Pancino et al. (2017) found that massive metal-poor clusters tend to have larger Al-Mg anticorrelations than their lighter counterparts. Nataf et al. (2019) used APOGEE data to show that the slope of the [Al/Fe] versus [N/Fe] relation depends on both metallicity and mass. Without dark matter, a globular cluster's ability to gather or retain material for star formation is tied directly to its stellar mass, and so (in a two-generation scenario) one might expect higher mass clusters to show more abundance variation, agreeing with the observations.

The corrected and uncorrected R_{Al} as a function of mass and absolute visual magnitude are plotted in the right-hand panels of Fig. 14. As significant Al spread was observed only in metal-poor clusters ([Fe/H]<-1.3), we explored the correlation between mass and R_{Al} for these metal-poor GCs separately from the metal-rich clusters. The correlation found, although moderate, is statistically significant both with mass and V_{ABS}, with $p = 0.0139$ and 0.0301, respectively. The appearance of correlation in both mass and V_{ABS} is trivial to understand because more massive clusters have higher luminosities. These results confirm previous literature findings for metal-poor GCs, however, high metallicity clusters with [Fe/H]>-1.3 do not have an obvious R_{Al}–mass correlation.

When looking at the R_{Al} dependence on mass and V_{abs} after the correction (bottom right-hand panels in Fig. 14) we find that the correlation appears more clearly, because the clusters are now not polluted by low Al FG stars. We therefore conclude that the extent of the enrichment of GCs stars is a function of both the cluster mass and metallicity, the correlation with mass becomes stronger when [Fe/H]<-1.3, while the correction removes most of the step from the metallicity dependence that is introduced because FG stars in low metallicity clusters have significantly lower [Al/Fe] than metal-rich clusters. This is in contrast with previous findings because the bias due to chemical evolution was not taken into account.

NGC 2808 and ω Cen are among the most massive accreted clusters in our sample. ω Cen does not exhibit larger Al enrichment than the rest of the clusters if the enrichment is plotted against the metallicity without the correction, which shows the importance of the correction. They separate more from the rest of the clusters when

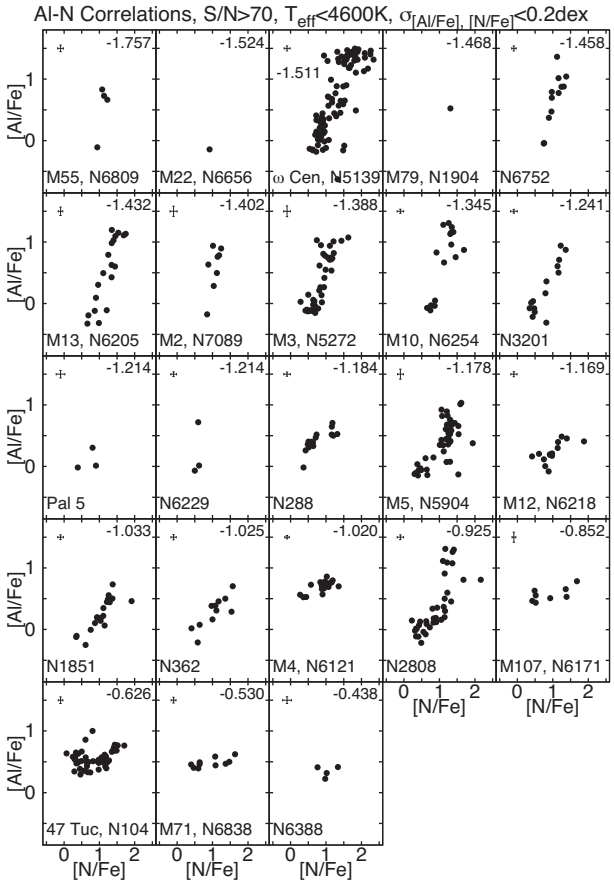

Figure 19. Al-N correlations. All cluster show clear Al-N correlations, except 47 Tuc, M4, M107, NGC 6388, and M71, cluster with no significant Al spread. Clusters are ordered by decreasing average metallicity, which is indicated in the top right-hand corner in each panel.

plotted against metallicity after the correction, because the extent of the Al enrichment in the SG stars is larger in more massive clusters.

6.3 Age

R_{Al} as a function of age (Krause et al. 2016) is plotted in Fig. 14. There are two distinctive groups visible in the R_{Al}−age diagram without the correction (upper panels), one is the metal-poor group ([Fe/H]<−1.3) for which there is no correlation between R_{Al} and age in the first three billion years, but that is only because our sample of GCs does not contain young, metal-rich clusters. The other one is the metal-rich group ([Fe/H]>−1.1) with low R_{Al}, and all of these clusters are older than 11.5 billion years. Again there seems to be no correlation with age in this group either. The lower left-hand panel shows the R_{Al}−age diagram after the correction, in which the metal-poor group only has a slightly larger scatter than the metal-rich ones. This is similar to what is shown in the metallicity panels.

6.4 Mg+Al+Si

The summed abundance of [(Mg+Al+Si)/Fe] is expected to be constant as a function of T_{eff} and that is what our results show in Fig. 15. Both FG and SG stars have the same [(Mg+Al+Si)/Fe] within the errors, and there are no density peaks observed in any of the clusters. The $R_{Mg+Al+Si}$ is very similar, or slightly larger than the average error of [(Mg+Al+Si)/Fe], which is what needs to be observed if the Mg-Al cycle operates normally. There seems to be no difference in [(Mg+Al+Si)/Fe] between *in situ* and accreted clusters.

As in previous sections, we explore the statistical significance of the correlation between the cluster properties and the sum and scatter of [(Mg+Al+Si)/Fe], shown in Fig. 16. There is a very minimal trend ($p = 0.0767$) between $R_{Mg+Al+Si}$ and metallicity, that is interpreted as errors of individual line fitting piling up with decreasing metallicity. Small correlations can appear on the level of the average error and usually are the result of correlated errors when the measured scatter is on the same level. When looking at the sum of [(Mg+Al+Si)/Fe] there are no such correlations present with metallicity, mass, or absolute visual magnitude, as expected. But there is a significant ($p = 0.0003$) correlation with age. This is due to a standard chemical evolution, which we confirmed by only looking at the statistics of FG stars that have halo-like chemical composition. This trend is dominated by [Mg/Fe] and [Si/Fe], which decreases as metallicity increases. This standard chemical evolution and structure of the Milky Way was recently overviewed by Hayden et al. (2015) and Weinberg et al. (2019) based on APOGEE data.

7 MULTIPLE POPULATIONS BASED ON N AND C

7.1 The N-C anticorrelation

C and N abundances are affected by two different astrophysical processes: (1) deep mixing occurring on the RGB, and (2) pollution from FG stars which is similar to the O-Na and Al-Mg patterns. Generally, N is anticorrelated with C in all observed clusters, but the slope of the anticorrelation is the combination of these two effects. The N-C and Al-O anticorrelations are shown in Figs 17 and 18, respectively. The Al-N correlation is plotted in Fig. 19, upper limits are omitted from the figures. Clusters with [Fe/H]<−1.8 dex are not plotted because the CO and CN lines in these stars are too weak to derive reliable abundances. The observed slopes were not corrected for deep mixing, but [C/Fe] is strongly correlated with temperature, a clear evidence of mixing occurring in every cluster.

The extended variations in N and C are observed in all GCs in our sample, in accordance with the earliest optical CH, CN, and NH observations (Norris 1987). There are several clusters in our sample that had no N-C anticorrelation published before: NGC 2808, M12, NGC 6229, M10, NGC 6388, and Pal 5, all of these exhibit clear N enhancements. Previous literature sources have reported both bimodal and continuous distributions of N abundances in GCs. Interestingly, multimodality cannot be easily identified in our data. This is because the number of stars with CN abundances is less than those with Mg and Al. There are two clusters in which bimodality can be convincingly determined: NGC 288 and M10. To a lesser extent, M5, NGC 3201, and M107 appear to have two distinctive populations based on N, but their existence is up to interpretation. All other clusters exhibit clear continuous distributions, which of course does not mean that multiple density peaks in the N-C plane, similar to that of Al-Mg, do not exist, but this can only be proved with more precise measurements of even more stars. M3 is an interesting case because it appears to have continuous N, but rather bimodal Al distribution (see Section 5.1), as reported by Mészáros et al. (2015).

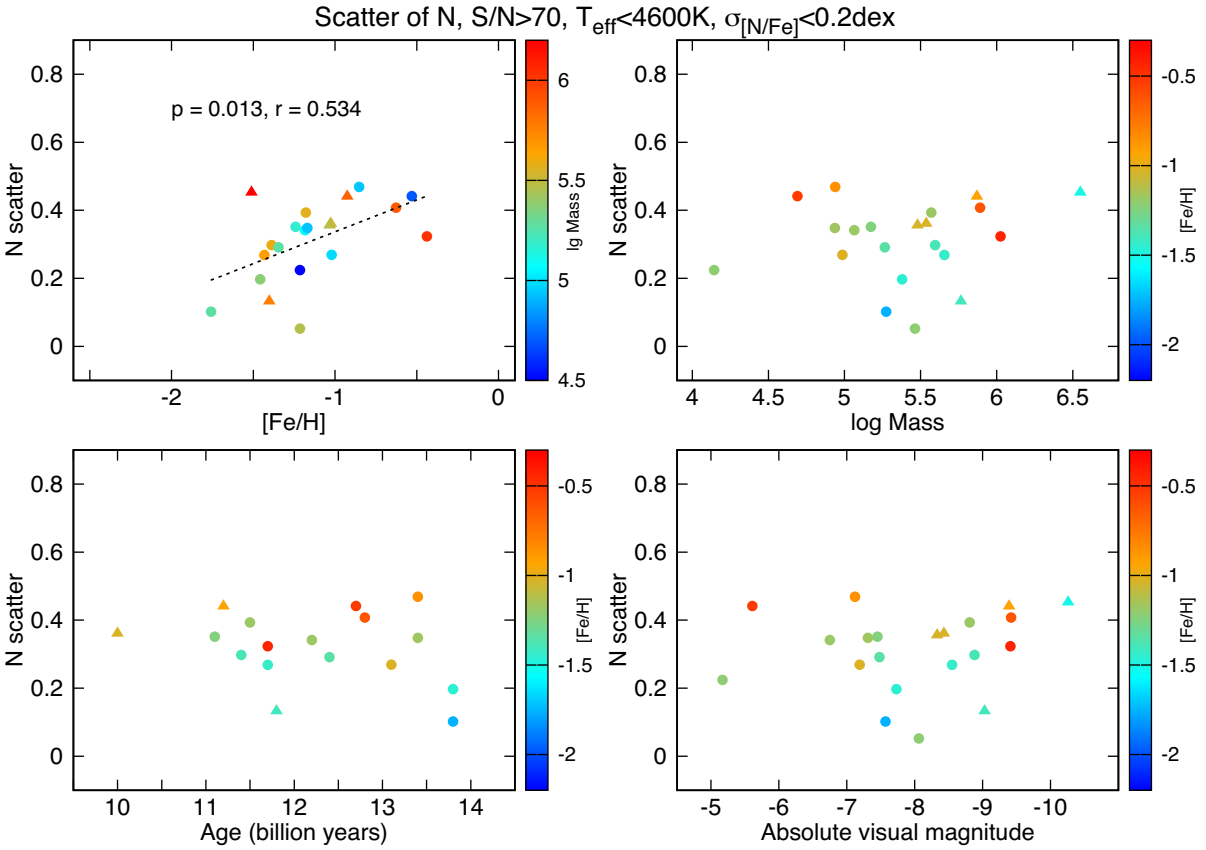

Figure 20. Scatter of N as a function of average cluster [Fe/H] colour coded by mass for clusters with at least three members. Accreted clusters are denoted by triangles, *in situ* clusters by solid circles.

7.2 The spread of N abundances

The scatter of N (R_N) as a function of [Fe/H] paints a very different picture from the scatter of Al, seen in Fig. 20. A correction to the Galactic evolution of N is not necessary, because N did not go through the same chemical evolution as Al (Hayes et al. 2018). Here, we observe a slight positive correlation ($p = 0.0126$) with metallicity. The number of stars for which the derivation of [N/Fe] is possible quickly decreases as metallicity decreases, because more and more stars are warmer and reach our determination limit of 4600 K and are the spectroscopic features also intrinsically weaker at lower metallicity. We required clusters to have at least three stars with [N/Fe] values to be included in this part of the analysis. This is somewhat offset by the expected increased errors at low metallicities, thus it is hard to judge how much these two systematics affect the correlation. The correlation remains even if we exclude the two most metal-poor GCs, thus focusing on the [Fe/H]>-1.5 region, in which these two sources of error are small. R_N does not appear to be correlated with either mass, V_{obs}, nor age. Also, it seems that both *in situ* and accreted clusters show similar R_N at the same metallicity.

As previously reported in the literature (Norris 1987) all metal-rich GCs have extended N distributions, even the ones with no significant Al scatter. This is the case for eight clusters in our sample: 47 Tuc, NGC 288, M4, M107, M12, NGC 6388, M71, and Pal 5. All these clusters have high metallicities, in which the Mg-Al cycle cannot start due to the polluting stars not reaching the necessary high temperatures in the stellar interiors. This can also be seen in the Al-N correlations and Al-O anticorrelations.

Al is expected to correlate with other elements produced during the proton-capture process, like Na and N, and anticorrelate with O and C. The Al-N and Al-O relationships (Figs 19 and 18) also help to identify whether pollution from the Mg-Al cycle occurred in the clusters with relatively low Al scatter, NGC 1851 and NGC 362. While their slightly increased R_{Al} values, 0.25 and 0.24, respectively, suggest some Al enhancement, only the Al-N and Al-O diagram can give convincing results by showing a clear (anti-)correlation between these abundances. NGC 288 and M12, two clusters with even lower R_{Al} values (0.18 and 0.16), that we assigned only one population to based on Al in Table 7, also seem to exhibit some Al-N anticorrelation, but only one of them, M12 has an Al-O anticorrelation. While NGC 288 and M12 are less certain to show Al pollution, the Al-Mg anticorrelation in these four clusters will need to be studied in a larger sample to reach more conclusive results on the parameter space in which the Mg-Al cycle contributes.

7.3 N spread in Clusters with no Al spread

In Section 6 we concluded that there are five metal-rich clusters in our sample that do not exhibit large Al-spread. These clusters are the following (from Table 7): 47 Tuc, M4, M107, NGC 6388, and M71. From Figs 18 and 19 we can conclude that these clusters have no clear Al-N correlation, or Al-O anticorrelations either, but clearly exhibit N-C anticorrelations (Fig. 17) and large N spreads (Fig. 20). M71 is particularly interesting because Ramírez & Cohen (2003) have observed a weak Al-Na correlation, and Yong,

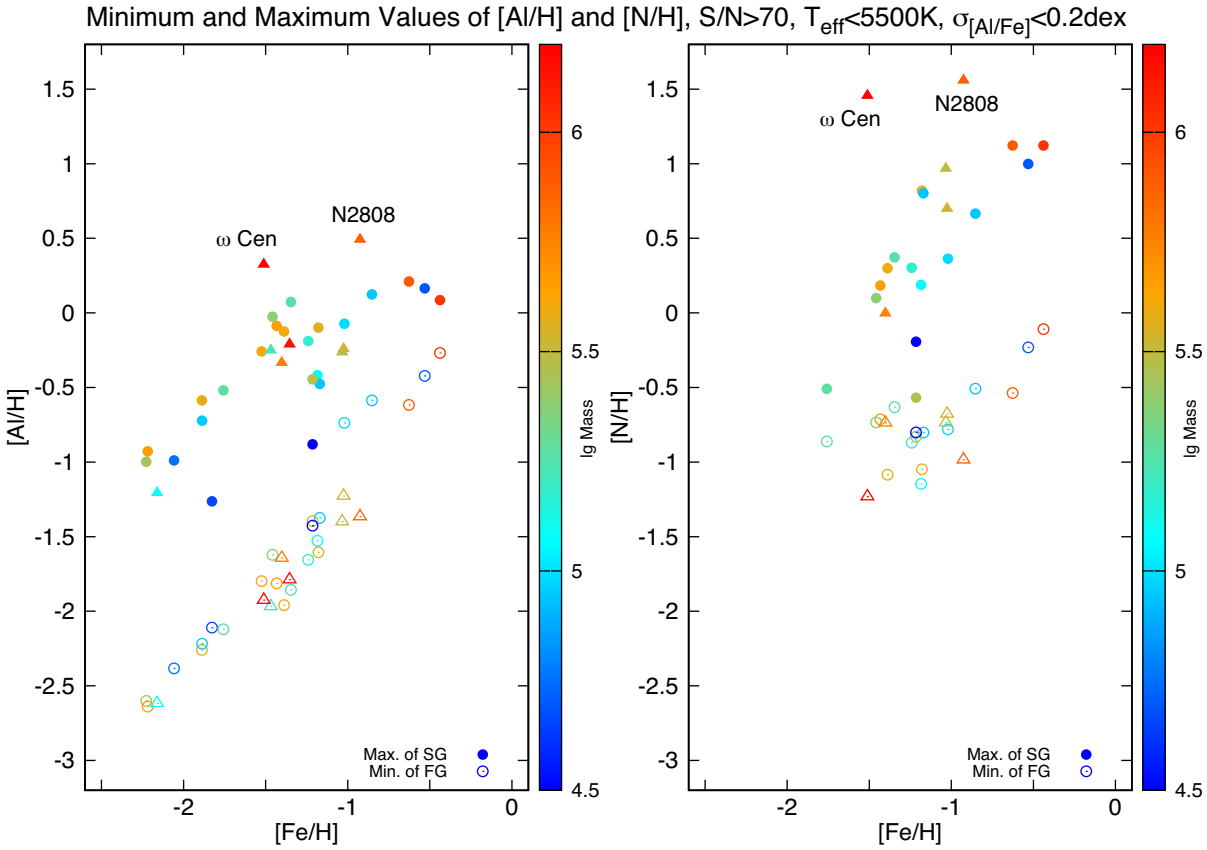

Figure 21. The maximum (solid symbols) and minimum (open symbols) values of [Al/H] and [N/H] in each cluster. Accreted clusters are denoted by triangles, *in situ* clusters by circles. The Al and N enrichment is strongest in the two massive accreted clusters ω Cen and NGC 2808.

Aoki & Lambert (2006) showed slightly non-standard isotope ratios suggesting some Mg-Al processing may have taken place. These clusters clearly have MPs based on their N abundances despite appearing to have single populations in the Al abundance. This is illustrated in Fig. 21, in which we plotted the minimum value of the [Al/H] and [N/H] in the FG stars by comparing it with the maximum value of [Al/H] and [N/H] in the SG stars as a function of metallicity. The extent of enrichment of Al is clearly the largest at the lowest metallicities and slowly decreases as metallicity increases, while the enrichment of N increases with increasing metallicty. The enrichment of Al and N is the largest in the two massive accreted clusters, ω Cen and NGC 2808, as previously found in Sections 6.1 and 7.2. We explore two different possible explanations of this observation.

The first explanation is as follows: because of the chemical evolution of Al, the FG stars in metal-rich clusters have already elevated [Al/Fe] abundances. This is not the case in the [N/Fe] dimension, since chemical evolution of N is not as steep as Al (Hayes et al. 2018). As mentioned in Section 6.1, when the [Al/Fe] of the FG stars are elevated, significantly more Al production is needed to be observable in the logarithmic abundance scale. Because of this it is entirely possible that Al production existed in these clusters (independent from the nature of the polluters), but did not reach the observable level, because the FG stars are mixed up with SG stars in the [Al/Fe] dimension. Both Schiavon et al. (2017) and Tang et al. (2017) have observed large Al spread in NGC 6553 using ASPCAP data, which is one of the most metal-rich GCs with [Fe/H] $= -0.15$ dex (Tang et al. 2017). NGC 6553 is also in our sample, but we excluded it from our analysis, because its reddening ($E(B-V) = 0.63$) is too high to derive reliable metallicities using photometric temperatures (see Section 4). These observations in M71 and NGC 6553 strongly supports this theory.

In the second case, the Mg-Al cycle is modest when [Fe/H]>-1 dex. If the GC polluters are massive AGB stars, we would expect a small Al production in the metal-rich clusters, because hydrogen burning in AGB stars operates at a higher temperature in lower metallicity stars, and so one might expect higher metallicity clusters to show less variation in elements that participate in the MgAl chain. Thus, in massive metal-rich AGB stars N variations are expected without, or very little, variation in Al, meaning that N is the best generation indicator for those metal-rich clusters. Indeed, this Al production dependence with metallicity has been used before to favour the massive AGB hypothesis (Ventura et al. 2016). This is supported by the dependence of Al on metallicity, which remains even after correcting for the standard chemical evolution discussed in Section 6.

The case of NGC 2808 is peculiar since it is a massive cluster with a large spread of Al and also has similar metallicity to these five clusters (47 Tuc, M4, M107, NGC 6388, and M71). One possible explanation is that NGC 2808 has not been formed in the Milky Way, such that Al was not high at the time of the formation and FG stars had lower Al than other clusters. At the same time other discussions regarding any pollution scenarios need detailed computations and analysis, which are far from the scope of the present investigation.

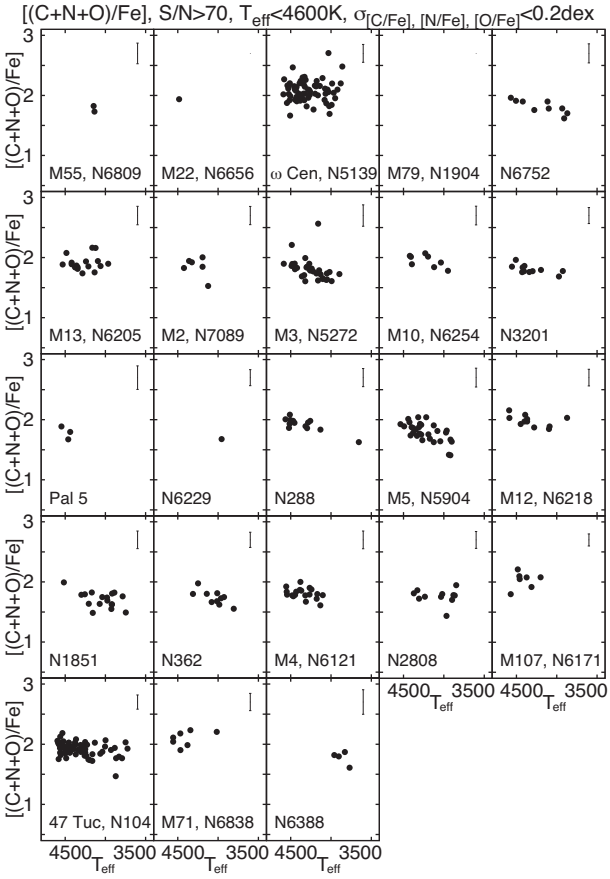

Figure 22. The C+N+O in each cluster is constant. Clusters are ordered by decreasing metallicity from left to right and top to bottom.

7.4 C+N+O

While deep mixing affects the C-N diagrams, the C+N+O should remain constant in each cluster as material is fully processed during the CNO cycle (Dickens, Croke & Cannon 1991). This is what we observe in all clusters, plotted as a function of $T_{\rm eff}$ in Fig. 22. Some slight correlations on the level of the average error can be seen in some clusters. However, these are most likely not of astrophysical origin, but the result of correlated errors between $T_{\rm eff}$ and CNO abundances. As previously mentioned, as temperature rises, the CN, CO, and OH lines become weaker and harder to measure.

The C+N+O cluster average is consistent with that observed in field stars at similar metallicities (Gratton et al. 2000). By looking at Fig. 23, no correlation with metallicity, mass, or $V_{\rm Abs}$ can be seen. *In situ* clusters do not have smaller or larger [(C+N+O)/Fe] than those captured via accretion. As with [(Mg+Al+Si)/Fe], the significant correlation between age and [(C+N+O)/Fe] is the result of standard chemical evolution and is dominated by [O/Fe].

An increase in the sum and also the scatter of CNO as a function of metallicity has been observed by Johnson & Pilachowski (2010) and by Marino et al. (2013). The increased scatter was the result of a dependence of C+N+O on [Fe/H]. While ω Cen will be discussed in detail in the third part of our series, we can briefly report that C+N+O is indeed larger than in other clusters ([(C+N+O)/Fe] = 2.07 dex). There is another cluster, M71, which has an even more elevated CNO sum, [(C+N+O)/Fe] = 2.09 dex. This is significantly higher than the typical value of [(C+N+O)/Fe], that varies from 1.7 to 2.0 dex in all but three clusters. The third is M107, [(C+N+O)/Fe] = 2.03 dex, but both clusters differ from ω Cen in that they are monometallic. M107 and M71 are part of those five clusters that do not have significant Al spread and their chemical evolution is more like that of the thick disc than the traditional halo (Fig. 12). The other three clusters (47 Tuc, M4, NGC 6388) have [(C+N+O)/Fe]<1.92 dex, so the sum of C+N+O does not become elevated for all metal-rich clusters.

The scatter of C+N+O ($R_{\rm CNO}$) shows a correlation with mass and $V_{\rm Abs}$. These are moderate correlations, with p = 0.013 and p = 0.0115, respectively. The average error of C+N+O spans a similar range to $R_{\rm CNO}$. Most of the correlation is the result of the increased C+N+O scatter of ω Cen, which is the most massive cluster in our sample. If ω Cen is not included in the fit, the statistical significance as a function of mass drops down dramatically to p = 0.0821 erasing most of the correlation. Thus, our conclusion is that there is no clear correlation between $R_{\rm CNO}$ and mass or $V_{\rm Abs}$.

8 OTHER ELEMENTS

8.1 Ca

All clusters are expected to have uniform and constant [Ca/Fe], because Ca is not affected by H-burning process as it is mostly produced by supernovae. This is what we see in our whole sample, Ca is constant in all clusters and its scatter is on the level of errors.

The only GC with a reported Ca spread is M22 (Marino et al. 2009), which was later disputed by Mucciarelli et al. (2015b) explaining the Ca spread with the presence of NLTE effects, similar to that of Fe discussed in Section 4.1. M22 is in our sample, however we were able to measure [Ca/Fe] in only a handful of stars, because the S/N of the M22 observations are low and Ca lines are generally weak at low metallicities. There are only three stars in our sample that satisfy the criteria set in Section 3.1 for analysis, and those three stars span a range of [Ca/Fe] = 0.35 to 0.5 dex, but two of those have errors of $\sigma_{\rm [Ca/Fe]}$ = 0.19 dex. These data are not sufficient to confirm or reject the findings of Marino et al. (2009).

8.2 Ce and Nd

S-process element enhancements are usually rare and are reported for only a few clusters (Marino et al. 2009; Roederer & Sneden 2011; Sobeck et al. 2011; Carretta et al. 2013; Marino et al. 2013; Shingles et al. 2014, M 22, M 15, M 92, M4, NGC 362, and NGC 1851). Nd II and Ce II lines have been discovered in the APOGEE spectral region by Hasselquist et al. (2016); Cunha et al. (2017). In Fig. 24, we show Ce and Nd abundances obtained from our sample. While there are only few constraining Nd measurements, we consider here stars with s-process enhancements such that [Ce/Fe]>0.4 based on the comparison with field stars measurement and our typical uncertainties. We can confirm s-process enhancement in all above-mentioned clusters except M22, for which our temperature cut-off do not leave any stars to be analysed. There is, however, several clusters in our sample with clear s-process enhancement: ω Cen NGC 362, NGC 1851, NGC 6760, and M4. ω Cen shows a clear increase of the Ce abundance as metallicity increases, confirming the early findings of Norris & Da Costa (1995) and supporting the pollution of this cluster by low mass AGB stars. In addition, we could identify one new cluster with s-process enhancement: NGC 6760 in which all three members show enhanced Ce.

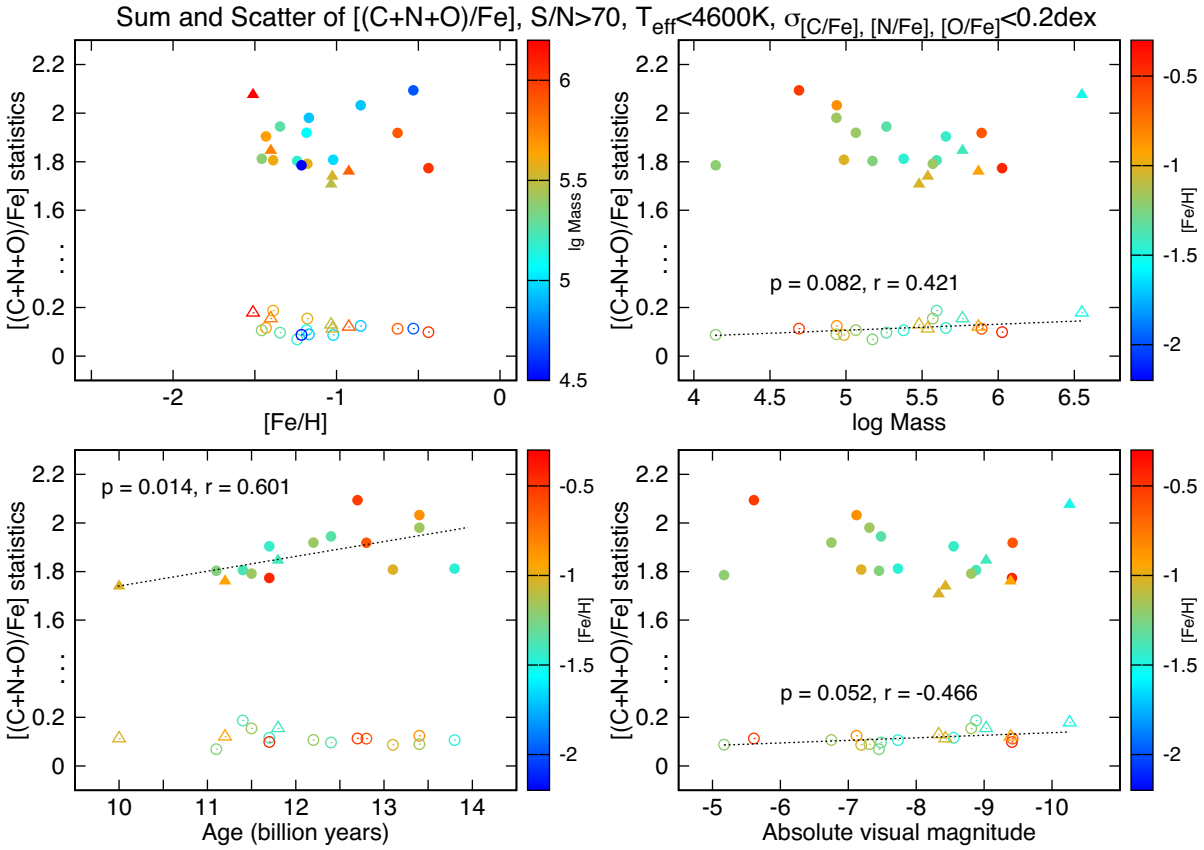

Figure 23. Statistics of C+N+O as a function of cluster [Fe/H] and mass. The filled symbols represent the average of C+N+O, the open symbols represent the scatter of C+N+O. The triangles are accreted clusters.

Masseron et al. (2019) discussed the case of M 15 and M 92 where they observe star-to-star variations of Ce compatible with the halo scatter. Consequently, they interpret that the Ce enhancement was inherited from the initial gas composition of the clusters. However, the other clusters with some s-process enhancement are more metal-rich than M15 and M92. At such metallicities, the Ce scatter in the field is much lower and the initial composition of the cluster gas can certainly be considered as homogeneous. Therefore, the s-process enhanced stars observed in M4, NGC 362, NGC 1851, and NGC 6760 (as well as ω Cen) have probably been polluted in Ce after the clusters have formed. Nevertheless, the presence of s-process rich stars is not correlated with the Al enhancement, nor it is with the cluster metallicity or the cluster mass. Thus, we believe that the s-process enrichment has been produced by a different source than the progenitor of the Mg-Al and Na-O anticorrelations, possibly by low-mass AGBs.

9 SUMMARY

In this paper we investigated the Fe, Mg, Al, C, N, and O abundances of 2283 red giant stars in 31 GCs from high-resolution spectra obtained by the SDSS-IV APOGEE-2 survey. We reported on the properties of MPs based on their Al-Mg, and C-N anticorrelations and also explored the dependence of the abundance spread of Fe, Al, and N on cluster properties. To summarize our results, we find the following:

(1) The scatter of Fe does not depend on mass, V_{Abs}, or age. The uncertainty coming from possible 3D/NLTE and reddening through photometric temperatures does not allow us to further refine the metallicity scale from the literature. By comparing three independent metallicity scales, we determine the metallicities of GCs derived from the H-band are 0.064 dex higher on average (in absolute terms) than the optical Fe scale.

(2) Other than the well-known Fe spread in ω Cen, we do not observe significant Fe variations in any of the clusters from our sample even though we have the precision to do so. This includes clusters with previously reported Fe spreads: M22, NGC 1851, and M54. While in M22 and NGC 1851 we have more than enough stars to sample multiple Fe populations, in M54 we only observed seven stars with S/N > 70. We most likely have not sampled enough stars with different Fe abundances, possibly due to limitations of the APOGEE fibre collision constraints which limit sampling the inner cluster regions.

(3) By using density maps of the Al-Mg anticorrelations we were able to identify multimodality in several clusters, including M79, ω Cen, and NGC 6752. While ω Cen and NGC 6752 were previously known to host more than two populations based on Al from the literature, M79 has not been previously reported on.

(4) In ω Cen, we observe a turnover in Al abundances for the most Mg-poor stars, similar to that of M15 and M92. Some of these Mg-poor stars are also slightly K enriched compared to standard FG stars drawing a weak K-Mg anticorrelation. However, the weak and blended K lines do not allow us to present a firm discovery of this K enrichment. Followup observations are needed to confirm or to contradict our findings.

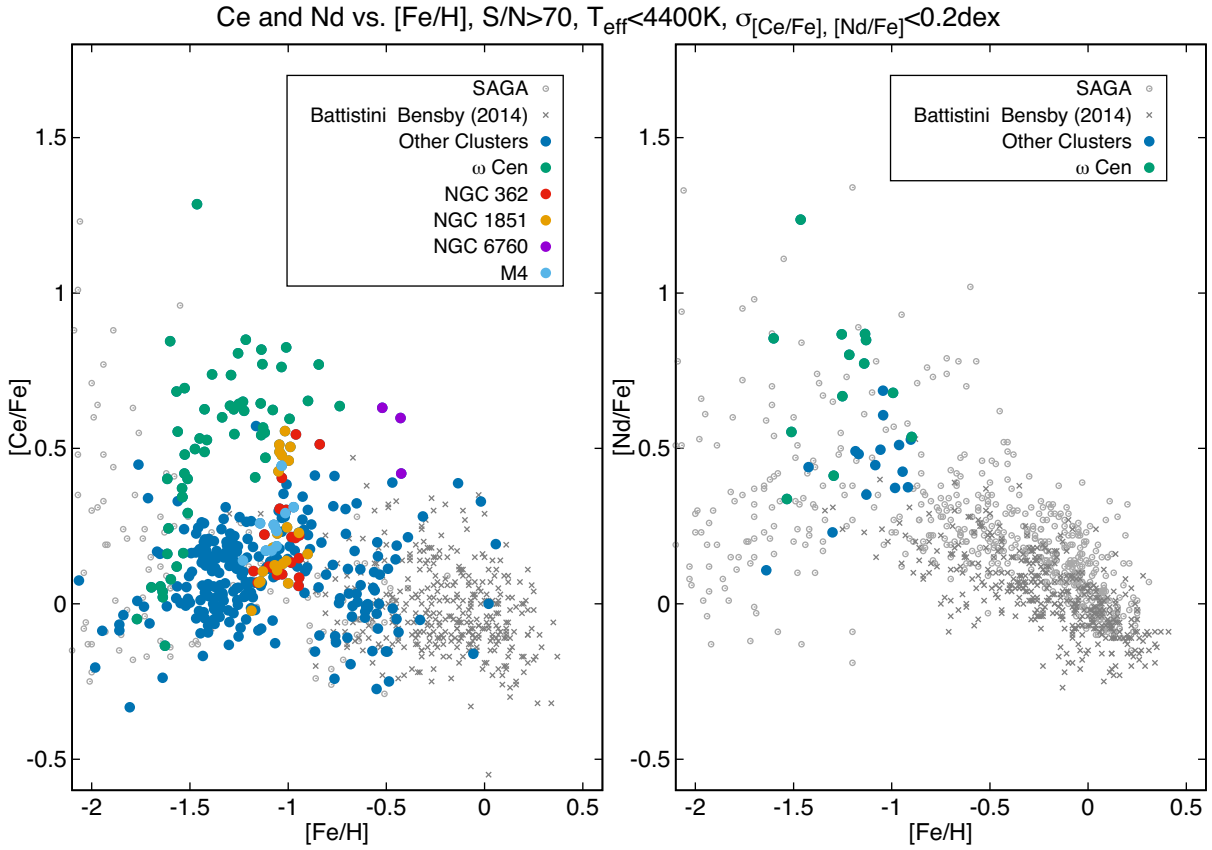

Figure 24. [Ce/Fe] and [Nd/Fe] as a function of metallicity for the sample stars. The background grey circles and crosses are field stars abundances extracted from the SAGA data base (Suda et al. 2008) and Battistini & Bensby (2016).

(5) We are able to confirm the Si-Mg anticorrelation observed in NGC 2808 by Carretta et al. (2009a), but the case of NGC 6752, as observed by Yong et al. (2005) is less convincing in our data.

(6) The ratio of the number of FG/SG stars depends on metallicity and age, but not on mass, which contradicts the findings of Milone et al. (2017). This may be explained by a sample bias created by selecting stars from the outer regions of the clusters which affects $f_{enriched}$ compared to *HST* studies which sampled the inner 2 arcmin of the clusters.

(7) We find a complex relationship between the spread of Al and cluster average metallicity and mass. We identified three distinctive groups in Al scatter – [Fe/H] diagram: (i) clusters with [Fe/H] < -1.3 have a near constant high R_{Al} value above 0.4 dex; (ii) clusters between $-1.0 <$ [Fe/H] < -1.3 show a wide variety of Al spread; (iii) the more metal-rich GCs have a small Al spread, comparable in size to the errors. This picture is changed when a correction for the chemical evolution of Al in the Milky Way is introduced. After the correction, the scatter of Al decreases and most of the large step between metal-poor and metal-rich clusters is removed, but the complex nature of the correlation with metallicity remains. The dependence of R_{Al} with cluster mass is increased suggesting that the extent of Al enrichment as a function of mass was suppressed before the correction.

(8) Metal-rich accreted clusters, NGC 2808 and ω Cen show significantly higher R_{Al} than their counterparts formed *in situ*. The rest of the accreted GCs appear to have similar Al spreads to the *in situ* clusters.

(9) The measured N-C anticorrelation is generally continuous with the exception of NGC 288 and M10, which show clear bimodality. This is in contrast with previous literature observations which generally found bimodal distributions.

(10) We measure constant Mg+Al+Si and C+N+O within all clusters. The sum does not depend on metallicity, mass, V_{Abs}, but on age, which is the result of standard chemical evolution. The scatter of Mg+Al+Si increases with decreasing metallicity which is most likely the result of accumulated errors at low metallicities. The scatter of C+N+O in ω Cen is larger than in other clusters, agreeing with previous literature finds.

(11) The five clusters (47 Tuc, M4, M107, NGC 6388, and M71) that have large variations in N, but Al scatter close to our uncertainties, appear to not show the signs of the Mg-Al cycle because their FG stars have elevated [Al/Fe] similar to thick disc stars. Considering that it is necessary to produce significantly more Al to reach the observational limit in the logarithmic abundance scale in metal-rich clusters than in metal-poor clusters, and the observations of Al-rich stars in NGC 6553 by Schiavon et al. (2017); Tang et al. (2017), we conclude that our observations of low Al scatter in these five clusters do not rule out the existence of the Mg-Al cycle.

(12) ω Cen shows a clear increase of the Ce abundance as metallicity increases, confirming the early findings of Norris & Da Costa (1995) and supporting the pollution of this cluster by low-mass AGB stars. We identified a new cluster, NGC 6760, with clear Ce enhancement.

ACKNOWLEDGEMENTS

SzM has been supported by the Premium Postdoctoral Research Program and János Bolyai Research Scholarship of the Hungarian Academy of Sciences, by the Hungarian NKFI Grants K-119517 and GINOP-2.3.2-15-2016-00003 of the Hungarian National Research, Development and Innovation Office. DAGH, TM, OZ, and FDA acknowledge support from the State Research Agency (AEI) of the Spanish Ministry of Science, Innovation and Universities (MCIU) and the European Regional Development Fund (FEDER) under grant AYA2017-88254-P. JGF-T is supported by FONDECYT No. 3180210. DG gratefully acknowledges support from the Chilean Centro de Excelencia en Astrofísicay Tecnologías Afines (CATA) BASAL grant AFB-170002. DG also acknowledges financial support from the Direccin de Investigacin y Desarrollo de la Universidad de La Serena through the Programa de Incentivo a la Investigacin de Acadmicos (PIA-DIDULS). TCB acknowledges partial support from grant PHY 14-30152; Physics Frontier Center/JINA Center for the Evolution of the Elements (JINA-CEE), awarded by the US National Science Foundation, and from the Leverhulme Trust (UK), during his visiting professorship at the University of Hull. SLM acknowledges the support of the Australian Research Council through Discovery Project grant DP180101791.

Funding for the Sloan Digital Sky Survey IV has been provided by the Alfred P. Sloan Foundation, the U.S. Department of Energy Office of Science, and the Participating Institutions. SDSS-IV acknowledges support and resources from the Center for High-Performance Computing at the University of Utah. The SDSS web site is www.sdss.org.

SDSS-IV is managed by the Astrophysical Research Consortium for the Participating Institutions of the SDSS Collaboration including the Brazilian Participation Group, the Carnegie Institution for Science, Carnegie Mellon University, the Chilean Participation Group, the French Participation Group, Harvard-Smithsonian Center for Astrophysics, Instituto de Astrofísica de Canarias, The Johns Hopkins University, Kavli Institute for the Physics and Mathematics of the Universe (IPMU) / University of Tokyo, Lawrence Berkeley National Laboratory, Leibniz Institut für Astrophysik Potsdam (AIP), Max-Planck-Institut für Astronomie (MPIA Heidelberg), Max-Planck-Institut für Astrophysik (MPA Garching), Max-Planck-Institut für Extraterrestrische Physik (MPE), National Astronomical Observatories of China, New Mexico State University, New York University, University of Notre Dame, Observatário Nacional / MCTI, The Ohio State University, Pennsylvania State University, Shanghai Astronomical Observatory, United Kingdom Participation Group, Universidad Nacional Autónoma de México, University of Arizona, University of Colorado Boulder, University of Oxford, University of Portsmouth, University of Utah, University of Virginia, University of Washington, University of Wisconsin, Vanderbilt University, and Yale University.

REFERENCES

Abadi M. G., Navarro J. F., Steinmetz M., 2006, MNRAS, 365, 747
Alonso A., Arribas S., Martinez-Roger C., 1999, A&AS, 140, 261
Alonso A., Arribas S., Martinez-Roger C., 2001, A&A, 376, 1039
Bastian N, Lardo C., 2015, MNRAS, 453, 357
Bastian N, Lardo C., 2018, ARA&A, 56, 83
Battistini C., Bensby T., 2016, A&A, 586, 49
Baumgardt H., Hilker M., 2018, MNRAS, 478, 1520
Baumgardt H., Hilker M., Sollima A., Bellini A., 2019, MNRAS, 482, 5138
Bekki K., Freeman K. C., 2003, MNRAS, 346, 11
Bertelli G., Girardi L., Marigo P., Nasi E., 2008, A&A, 484, 815
Bertelli G., Nasi E., Girardi L., Marigo P., 2009, A&A, 508, 355
Blanton M. R. et al., 2017, AJ, 154, 28
Bullock J. S., Johnston K. V., 2005, ApJ, 635, 931
Carretta E., Bragaglia A., Gratton R., Lucatello S., 2009a, A&A, 505, 139
Carretta E. et al., 2009b, A&A, 505, 117
Carretta E., Bragaglia A., Gratton R., D'Orazi V., Lucatello S., 2009c, A&A, 508, 695
Carretta E. et al., 2010a, ApJ, 714, L7
Carretta E. et al., 2010b, A&A, 516, 55
Carretta E., Bragaglia A., Gratton R. G., Lucatello S., D'Orazi V., 2012, ApJ, 750, L14
Carretta E. et al., 2013, A&A, 557, 138
Cohen J. G., Briley M. M., Stetson P. B., 2002, AJ, 123, 2525
Cunha K. et al., 2017, ApJ, 844, 145
Da Costa G. S., et al., 2016, in Bragaglia A., ed, IAU Symp. 317, The General Assembly of Galaxy Haloes: Structure, Origin and Evolution. Cambridge Univ. Press, Cambridge, p. 110
de Mink S. E., Pols O. R., Langer N., Izzard R. G., 2009, A&A, 507, L1
Decressin T., Meynet G., Charbonnel C., Prantzos N., Ekström S., 2007, A&A, 464, 1029
Denissenkov P. A., Hartwick F. D. A., 2014, MNRAS, 437, L21
Dickens R., Croke B., Cannon R., Bell R., 1991, Nature, 351, 212
Eisenstein D. J. et al., 2011, AJ, 142, 72
Fernández-Trincado J. G. et al., 2019, A&A, 627, 178
Font A. S., Johnston K. V., Bullock J. S., Robertson B. E., 2006, ApJ, 638, 585
Forbes D. A., Bridges T., 2010, MNRAS, 404, 1203
Gaia Collaboration 2018, A&A, 616, A1
García Pérez A. E. et al., 2016, AJ, 151, 144
García-Hernández D. A. et al., 2015, ApJ, 815, L4
Gilmore G. et al., 2012, Messenger, 147, 25
González Hernández J. I., Bonifacio P., 2009, A&A, 497, 497
Gratton R. G., Sneden C., Carretta E., Bragaglia A., 2000, A&A, 354, 169
Gratton R. G. et al., 2001, A&A, 369, 87
Gratton R. G., Carretta E., Claudi R., Lucatello S., Barbieri M., 2003, A&A, 404, 187
Gratton R. G., Johnson C. I., Lucatello S., D'Orazi V., Pilachowski C., 2011, A&A, 534, 72
Gratton R. G., Carretta E., Bragaglia A., 2012, A&A Rev., 20, 50
Grevesse N., Asplund M., Sauval A. J., 2007, Space Sci. Rev., 130, 105
Gunn J. E. et al., 2006, AJ, 131, 2332
Harris W. E., 1996, AJ, 112, 1487
Hasselquist S. et al., 2016, ApJ, 833, 81
Hayden M. R. et al., 2015, ApJ, 808, 132
Hayes C. R. et al., 2018, ApJ, 852, 49
Holtzman J. A., Shetrone M., Johnson J. A., 2015, AJ, 150, 148
Holtzman J. A., Hasselquist S., Shetrone M., 2018, AJ, 156, 125
Ivans I. I. et al., 2001, AJ, 122, 1438
Johnson C. I., Pilachowski C. A., 2010, ApJ, 722, 1373
Jönsson H. et al., 2018, AJ, 156, 126
Kraft R. P., Sneden C., Langer G. E., Prosser C. F., 1992, AJ, 104, 645
Kraft R. P., Sneden C., Langer G. E., Shetrone M. D., Bolte M., 1995, AJ, 109, 2586
Krause M. G. H., Charbonnel C., Bastian N., Diehl R., 2016, A&A, 587, 53
Lardo C., Mucciarelli A., Bastian N., 2016, MNRAS, 457, 51
Maccarone T. J., Zurek D. R., 2012, MNRAS, 423, 2
Majewski S. R. et al., 2017, AJ, 154, 94
Marigo P. et al., 2017, ApJ, 835, 77
Marín-Franch A. et al., 2009, ApJ, 694, 1498
Marino A. F. et al., 2009, A&A, 505, 1099
Marino A. F. et al., 2011, ApJ, 731, 64
Marino A. F. et al., 2014, MNRAS, 442, 3044
Massari D. et al., 2014, ApJ, 795, 22
Masseron T., Merle T., Hawkins K., 2016, Astrophysics Source Code Library, record ascl:1605.004
Masseron T. et al., 2019, A&A, 622, 191
Meszaros Sz. et al., 2013, AJ, 146, 133
Mészáros S. et al., 2015, AJ, 149, 153

Mészáros S. et al., 2018, MNRAS, 475, 1633
Milone A. P., 2015, MNRAS, 446, 1672
Milone A. P. et al., 2017, MNRAS, 464, 3636
Mucciarelli A. et al., 2012, MNRAS, 426, 2889
Mucciarelli A. et al., 2015a, ApJ, 801, 68
Mucciarelli A. et al., 2015b, ApJ, 809, 128
Myeong G. C., Evans N. W., Belokurov V., Sanders J. L., Koposov S. E., 2018, ApJ, 863, 28
Nataf D. M. et al., 2019, AJ, 158, 14
Nidever D. L. et al., 2015, AJ, 150, 173
Nidever D. L. et al., 2019, preprint (arXiv:1901.03448)
Norris J., 1987, ApJ, 313, L65
Norris J. E., Da Costa G. S., 1995, ApJ, 447, 680
Pancino E. et al., 2017, A&A, 601, 112
Peñarrubia J., Walker M. G., Gilmore G., 2009, MNRAS, 399, 1275
Piotto G. et al., 2007, ApJ, 661, L53
Piotto G. et al., 2015, AJ, 149, 91
Ramírez S. V., Cohen J. G., 2003, AJ, 125, 224
Roederer I. U., Sneden C., 2011, AJ, 142, 22
Sarajedini A. et al., 2007, AJ, 133, 1658
Schiavon R. P. et al., 2017, MNRAS, 466, 1010
Shetrone M. D., 1996, AJ, 112, 1517
Shingles L. J. et al., 2014, ApJ, 795, 34
Sneden C., Kraft R. P., Prosser C. F., Langer G. E., 1991, AJ, 102, 2001
Sneden C., Kraft R. P., Prosser C. F., Langer G. E., 1992, AJ, 104, 2121
Sneden C. et al., 1997, AJ, 114, 1964
Sneden C., Pilachowski C. A., Kraft R. P., 2000, AJ, 120, 1351
Sneden C., Kraft R. P., Guhathakurta P., Peterson R. C., Fulbright J. P., 2004, AJ, 127, 2162
Sobeck J. S. et al., 2011, AJ, 141, 175
Soto M. et al., 2017, AJ, 153, 19
Stetson P. B., Pancino E., Zocchi A., Sanna N., Monelli M., 2019, MNRAS, 485, 3042
Suda T. et al., 2008, PASJ, 60, 1159
Tang B. et al., 2017, MNRAS, 465, 19
Ventura P., D'Antona F., Mazzitelli I., Gratton R., 2001, ApJ, 550, L65
Ventura P. et al., 2012, ApJ, 761L, 30
Ventura P. et al., 2016, ApJ, 831, L17
Weinberg D. H. et al., 2019, ApJ, 874, 102
Yong D., Grundahl F., Nissen P. E., Jensen H. R., Lambert D. L., 2005, A&A, 438, 875
Yong D., Aoki W., Lambert D. L., 2006, ApJ, 638, 1018
Yong D. et al., 2014, MNRAS, 441, 3396
Zasowski G. et al., 2013, AJ, 146, 81
Zasowski G. et al., 2017, AJ, 154, 198

SUPPORTING INFORMATION

Supplementary data are available at *MNRAS* online.

Table 2. Atmospheric parameters and abundances of individual stars.

Please note: Oxford University Press is not responsible for the content or functionality of any supporting materials supplied by the authors. Any queries (other than missing material) should be directed to the corresponding author for the article.

[1]*ELTE Eötvös Loránd University, Gothard Astrophysical Observatory, 9700 Szombathely, Szent Imre H. st. 112, Hungary*
[2]*Premium Postdoctoral Fellow of the Hungarian Academy of Sciences*
[3]*MTA-ELTE Exoplanet Research Group, 9700 Szombathely, Szent Imre h. st. 112, Hungary*
[4]*Instituto de Astrofísica de Canarias (IAC), La Laguna, E-38205 Tenerife, Spain*
[5]*Universidad de La Laguna (ULL), Departamento de Astrofísica, La Laguna, E-38206 Tenerife, Spain*
[6]*Department of Physics and JINA Center for the Evolution of the Elements, University of Notre Dame, Notre Dame, IN 46556, USA*
[7]*Apache Point Observatory, PO Box 59, Sunspot, NM 88349, USA*
[8]*Department of Astronomy, New Mexico State University, Las Cruces, NM 88003, USA*
[9]*Space Telescope Science Institute, 3700 San Martin Drive, Baltimore, MD 21218, USA*
[10]*Steward Observatory, University of Arizona, 933 North Cherry Avenue, Tucson, AZ 85721, USA*
[11]*Observatório Nacional, 77 Rua General José Cristino, Rio de Janeiro, 20921-400, Brazil*
[12]*Department of Astronomy, University of Virginia, Charlottesville, VA 22904-4325, USA*
[13]*Instituto de Astronomía y Ciencias Planetarias, Universidad de Atacama, Copayapu 485, Copiapó, Chile*
[14]*Institut Utinam, CNRS-UMR 6213, Université Bourgogne-Franche-Compté, OSU THETA Franche-Compté, Observatoire de Besançon, BP 1615, F-251010 Besançon Cedex, France*
[15]*Department of Physics & Astronomy, Texas Christian University, Fort Worth, TX 76129, USA*
[16]*Departamento de Astronomía, Universidad de Concepción, Casilla 160-C, Concepción, Chile*
[17]*Instituto de Investigacin Multidisciplinario en Ciencia y Tecnología, Universidad de La Serena. Avenida Ral Bitrn S/N, La Serena, Chile*
[18]*Departamento de Astronomía, Facultad de Ciencias, Universidad de La Serena. Av. Juan Cisternas 1200, La Serena, Chile*
[19]*Department of Physics and Astronomy, University of Utah, Salt Lake City, UT 84112, USA*
[20]*Department of Astronomy and Astrophysics, The Pennsylvania State University, University Park, PA 16802, USA*
[21]*New Mexico State University, Las Cruces, NM 88003, USA*
[22]*Department of Astronomy, The Ohio State University, 140 W. 18th Ave., Columbus, OH 43210, USA*
[23]*Instituto de Astroísica, Pontificia Universidad Catalica de Chile, Av. Vicuna Mackenna 4860, Macul, 782-0436 Santiago, Chile*
[24]*Instituto Milenio de Astrofísica, Av. Vicuña Mackenna 4860, Macul, 782-0436 Santiago, Chile*
[25]*Centro de Astronomia, Universidad de Antofagasta, Avenida Angamos 601, Antofagasta 1270300, Chile*
[26]*School of Physics, University of New South Wales, NSW 2052, Australia*
[27]*Departamento de Ciencias Fisicas, Facultad de Ciencias Exactas, Universidad Andres Bello, Av. Fernandez Concha 700, Las Condes, Santiago, Chile*
[28]*Millennium Institute of Astrophysics, Av. Vicuna Mackenna 4860, 782-0436 Santiago, Chile*
[29]*Vatican Observatory, I-V00120 Vatican City State, Italy*
[30]*Department of Physics and Astronomy, Johns Hopkins University, Baltimore, MD 21218, USA*
[31]*Department of Physics, Montana State University, PO Box 173840, Bozeman, MT 59717-3840, USA*
[32]*National Optical Astronomy Observatory, 950 North Cherry Avenue, Tucson, AZ 85719, USA*
[33]*Astrophysics Research Institute, IC2, Liverpool Science Park, Liverpool John Moores University, 146 Brownlow Hill, Liverpool L3 5RF, UK*
[34]*University of Texas at Austin, McDonald Observatory, Fort Davis, TX 79734, USA*
[35]*Center for Astrophysics and Space Astronomy, Department of Astrophysical and Planetary Sciences, University of Colorado, 389 UCB, Boulder, CO 80309-0389, USA*
[36]*School of Physics and Astronomy, Sun Yat-sen University, Zhuhai, China*

This paper has been typeset from a TEX/LATEX file prepared by the author.